AGU ADVANCING EARTH AND SPACE SCIENCES

JGR Solid Earth

RESEARCH ARTICLE
10.1029/2025JB033462

GIA-Induced Mantle Circulation and Surface Horizontal Motions in North America: Effects of 3D Laterally Varying Elastic Thickness and Viscosity

Kaixuan Kang[1] and **Thorsten W. Becker**[1,2,3]

[1]Jackson School of Geosciences, Institute for Geophysics, The University of Texas at Austin, Austin, TX, USA, [2]Department of Earth and Planetary Sciences, Jackson School of Geosciences, The University of Texas at Austin, Austin, TX, USA, [3]Oden Institute for Computational Engineering and Sciences, The University of Texas at Austin, Austin, TX, USA

Key Points:

- Horizontal crustal motions show a delayed response to the onset of deglaciation and subsequent reversal in motion
- The reversal timing is controlled by elastic lithospheric flexure and viscous mantle response
- A weak asthenosphere channels mantle flow, forming a "box-like" circulation beneath the former ice cover

Supporting Information:

Supporting Information may be found in the online version of this article.

Correspondence to:

K. Kang,
kaixuankang@tongji.edu.cn

Citation:

Kang, K., & Becker, T. W. (2026). GIA-induced mantle circulation and surface horizontal motions in North America: Effects of 3D laterally varying elastic thickness and viscosity. *Journal of Geophysical Research: Solid Earth*, *131*, e2025JB033462. https://doi.org/10.1029/2025JB033462

Received 22 NOV 2025
Accepted 24 JUL 2026

Author Contributions:

Conceptualization: Thorsten W. Becker
Data curation: Kaixuan Kang
Formal analysis: Kaixuan Kang
Funding acquisition: Thorsten W. Becker
Investigation: Kaixuan Kang
Methodology: Kaixuan Kang
Project administration: Thorsten W. Becker
Supervision: Thorsten W. Becker
Validation: Kaixuan Kang
Visualization: Kaixuan Kang
Writing – original draft: Kaixuan Kang

Abstract The horizontal surface motions of the Earth's crust induced by glacial isostatic adjustment (GIA) are highly sensitive to lateral variations in Earth properties. We construct 3D GIA models by incorporating both varying elastic lithospheric thickness and lateral viscosity variations in the asthenosphere in a global, compressible, self-gravitating, viscoelastic Earth model. This allows us to investigate how geological structures such as the North American continental craton with thick lithosphere and stiff upper mantle and oceanic plate regions with thinner lithosphere and weak asthenosphere influence mantle flow during and after the last deglaciation and how this relaxation is expressed in surface motions. While vertical crustal motions are always in phase with the ice loading change, horizontal motions can be out of phase with the glaciation history and vertical motions. The delay in response to deglaciation and the timing of the direction reversal after deglaciation is complete are controlled by the interplay between elastic lithospheric flexure and the mantle viscous drag on the base of the lithosphere. The weak asthenosphere channels the mantle return flow more horizontally and the stiff cratonic root directs the flow more vertically, forming a "box-like" circulation beneath the former ice cover. Such complex interactions may be better constrained with joint geodetic and seismic anisotropy analysis and provide new perspectives for GIA-ice sheet interactions as well as the interpretation of GIA associated seismotectonics.

Plain Language Summary During the last ice age, massive ice sheets accumulated transiently over North America, inducing mantle flow first away from and then back toward the ice center with delayed surface deformation. After the ice melting was completed, surface crustal vertical motions show uplift around the former ice center with diminished amplitude over time, while horizontal velocities show reversals in direction, including a transition from inward to outward motion. The crustal deformation patterns and the reversal timing for horizontal motions are controlled by the interplay between the elastic lithosphere and the viscous mantle. Lateral variations in Earth structure, such as variable lithosphere thickness and mantle viscosity between the continental root and oceanic plate, lead to distinct mantle flow beneath the former ice center, resulting in complex surface horizontal motion.

1. Introduction

During the Last Glacial Maximum (LGM, ~21–26 ka), most of North America was covered by the Laurentide, Cordilleran, and Innuitian ice sheets, with thickness exceeding 3–4 km over Hudson Bay and central Canada, with its southern margin extending well beyond the US-Canadian border (Figure 1). The ice sheet collapsed and retreated rapidly in response to abrupt climate events, such as Meltwater Pulse1A (MWP1A, ~14 ka) and 1B (MWP1B, ~11 ka) and largely disappeared by the mid-Holocene warming at ~6–7 ka. The changes in ice mass and the associated redistribution of ocean mass impose surface loading variations that drove viscoelastic deformation of the solid Earth, a process known as glacial isostatic adjustment (GIA; Farrell & Clark, 1976; Peltier & Andrews, 1976).

GIA is a combination of the instantaneous elastic response at the loading time and a time-delayed viscous response that continues to the present day, traditionally inferred from shoreline uplift, but also as currently seen by Global Navigation Satellite System (GNSS) observations; those show uplift rates exceeding 10 mm/yr near the former ice centers (e.g., Hudson Bay) and subsidence (~1–2 mm/yr) around the peripheral bulge (e.g., the Atlantic coast of North America). The observed horizontal velocities within the former ice cover show a

Writing – review & editing:
Kaixuan Kang, Thorsten W. Becker

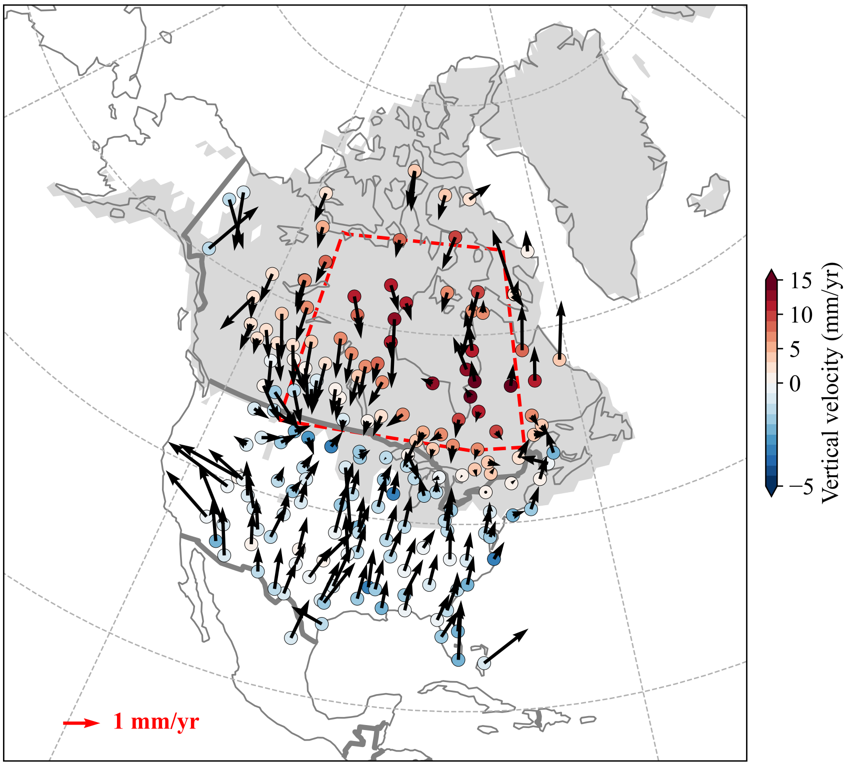

Figure 1. Selected GNSS vertical and horizontal velocities in North America from Argus et al. (2021) focusing on regions away from active plate boundary deformation. The gray shading denotes the extent of LGM ice cover. The dashed red frame indicates the region used for regional average calculations. Country borders are also shown.

combination of southern motion in western and southern Canada and northern motion across eastern Canada, while velocities beyond the former ice margin and in the far field, including most of the United States, also point north (Figure 1; Argus et al., 2021). The ongoing GIA signal is important for a range of solid Earth-cryosphere interactions, including disentangling contemporary processes such as hydrological variations, deformation throughout the seismic cycle, and mantle driven signatures in geodetic observations of surface deformation (e.g., Husson et al., 2018; Kreemer et al., 2018; Lau et al., 2020; Snay et al., 2016; Vardic et al., 2022).

The main parameters controlling the GIA process are the forcing due to the glaciation history and Earth structure, in particular the viscoelastic behavior of the solid Earth including depth-dependent elastic and viscous properties. However, rock deformation experiments, geological and geophysical observations, and geodynamic modeling also indicate significant lateral variations in rock properties, in particular in the upper ∼400 km of the mantle. Those include variable lithospheric elastic and thermal thickness (e.g., Audet & Bürgmann, 2011; Bechtel et al., 1990; Steinberger & Becker, 2018; Watts et al., 2013; Zhong et al., 2003), and lateral viscosity variations in the mantle (e.g., Becker, 2006; Osei Tutu et al., 2018; Ricard et al., 1991; van Summeren et al., 2012; Zhong, 2001). Therefore, GIA models with relative sea level (RSL) records and GNSS constraints based on 1D Earth structure often yield different estimates of best-fit lithosphere thickness and mantle viscosity (e.g., Barletta et al., 2018; James et al., 2009; Kang et al., 2025; Lau et al., 2016; Nield et al., 2014; Parang et al., 2024; Yousefi et al., 2018). Such discrepancies highlight the limitations of representing local Earth structure with 1D models and a requirement for 3D structure that can capture the spatial variability of rheological features in different regions of the Earth.

For example, considering RSL data subset. along the Pacific coast of central North America (e.g., Yousefi et al., 2018) and along the Atlantic coast of North America (e.g., Parang et al., 2024), model misfit can be reduced if viscosity is allowed to vary regionally. Such studies indicate RSL observations sense lateral variations in Earth structure, emphasizing the necessity for incorporating 3D structure in GIA models to interpret observations (e.g., Kaufmann & Wu, 1998; Latychev et al., 2005; Paulson et al., 2005).

A number of studies on 3D GIA models have thus been conducted to quantify the impact of lateral heterogeneity on GIA predictions (e.g., Crawford et al., 2018; Gasperini et al., 1991; Kaufmann et al., 2000; Latychev et al., 2005; Steffen et al., 2006, 2008; Wu, 2005; Zhong et al., 2003, 2022), and improve the fit between GIA models and observations (e.g., Wahr and Zhong, 2013; Li et al., 2018, 2020; Yousefi et al., 2021; Bagge et al., 2021; Parang et al., 2024, for RSL, and van der Wal et al., 2015, for GNSS data). However, there are remaining disagreements regarding the extent to which laterally varying Earth structure dominates surface deformation and how much incorporating such structures improves the interpretations of geodetic and geological observations.

The sensitivity of GIA observables to lateral Earth structure has been investigated in several studies. Gasperini et al. (1990) found that horizontal displacements are more sensitive to lateral variations in the viscosity of the lithosphere and upper mantle than vertical displacements. Milne et al. (2004) mostly observed a decrease in sensitivity from the shallow upper mantle to deeper parts in Fennoscadia. Wu (2006) constructed sensitivity kernels for RSL and crustal velocities in the Laurentide region and emphasized that horizontal velocities are sensitive to viscosity variations in the shallow mantle directly beneath the ice load. However, Steffen et al. (2007) investigated the sensitivity of crustal velocities in Fennoscandia and showed that lateral structure within the lower part of the upper mantle, around ∼450–670 km depth, have the strongest influence on horizontal motion. Steffen and Wu (2014) further quantified that GNSS stations are most sensitive to viscosity changes directly beneath the station, primarily at depths between 250 and 550 km. With few exceptions, stations within the former ice margin show the greatest sensitivity to local viscosity within a lateral extent of 250 km, whereas stations outside the formerly glaciated area lack sufficient sensitivity to viscosity directly beneath them (Steffen & Wu, 2014). Lau et al. (2018) substantiated the importance of the bottom half of the upper mantle by examining the sensitivity kernels for the Fennoscandian relaxation spectrum (FRS), postglacial decay times in Canada and Scandinavia, and the rate of change of the degree-2 zonal harmonic of the geopotential. These remaining disagreements between previous studies highlight the complexity of how lateral heterogeneity in Earth structure modulates mantle flow at different depths and its surface deformation signature.

Regarding improvements in fitting geodetic observations, van der Wal et al. (2015) found that 3D models provided a better fit to GNSS uplift rates in Antarctica than 1D, and Li et al. (2022) showed that 3D model predictions of RSL largely resolve the misfits with observed data from the White Sea in the Russian Arctic. By tuning the strength of 3D viscosity variations, Wang et al. (2008), Steffen et al. (2008), Li et al. (2018), and Bagge et al. (2021) demonstrated that introducing lateral heterogeneity within a certain range of variations can help resolve some misfits in RSL and/or geodetic data. In contrast, Steffen et al. (2006) and Kierulf et al. (2014) found that 3D models perform satisfactorily to fit the GNSS observations in Fennoscandia but not as well as the best fitting 1D models. Yousefi et al. (2021) suggest that their 3D models do not yield clear improvement in fitting RSL observations along the Pacific coast of North America, and Parang et al. (2024) found that 3D models failed to enhance the data-model fits relative to 1D model in eastern North America. These discrepancies highlight the limitations and uncertainties in current 3D GIA models and suggest the need for a better understanding of the physics of how surface loading induced viscous flow within a laterally varying Earth affects surface observables.

Here, we focus on the mix between horizontal and vertical surface deformation as constraints. In GIA modeling, the lithosphere is often defined as a very high viscosity viscoelastic layer which behaves essentially elastically over GIA timescales. Elastic flexure of the lithosphere is modulated by underlying mantle flow which affects the pattern and amplitude of surface motions. While the vertical motions associated with GIA have been extensively studied and show consistency among models overall, horizontal motions remain less well explored and exhibit larger discrepancies across studies. Horizontal motions are more difficult to interpret than vertical motion in GNSS observations because their amplitudes are typically 4–5 times smaller and more variable across GIA models, reflecting their sensitivity to shallow Earth structure and ice model details. Moreover, it is crucial to use a compressible viscoelastic solution for accurate estimates of horizontal deformation (Johnston et al., 1997; Mitrovica et al., 1994; Reusen et al., 2023; Tanaka et al., 2011), and open-source codes capable of fully capturing such 3D deformation along with solving the sea level equation have only recently become widely available (Yuan et al., 2025; Zhong et al., 2022).

James and Morgan (1990) were among the first to consider horizontal motions in 1D GIA models. They predicted converging horizontal motion around Hudson Bay and attributed this pattern to return flow in the sub-lithospheric mantle that drags the overlying lithosphere with it. James and Lambert (1993) reported that the inclusion of compressibility in their spherical model predicted divergent motions around Hudson Bay instead. Mitrovica et al. (1994) and Milne et al. (2001) predicted divergent horizontal motion around previous ice centers (e.g., Hudson Bay and Fennoscandia) by using a more realistic Earth model and ice history, results that are more consistent with modern geodetic observations (Kreemer et al., 2018; Sella et al., 2007; Vardić et al., 2022), in particular for Fennoscandia (e.g., Milne et al., 2001). Argus and Peltier (2010) found that by introducing a 40 km thick sub-lithospheric, high viscosity (10^{22} Pas) layer, the 1D model misfit of horizontal motions in North America is greatly improved.

With a 3D Earth model, Kaufmann et al. (2005) studied the crustal motions induced by late-Pleistocene ice-sheet distributions in Antarctica and found that horizontal flow patterns are controlled by the flow from the stiff East Antarctic cratonic root to the weaker West Antarctic mantle and low seismic velocity zones beneath the adjacent oceanic plate regions. Wu (2005) and Wang and Wu (2006) found that lateral heterogeneity has large effects on horizontal motions and can completely overprint the divergent pattern of flow predicted by laterally homogeneous models in Laurentia. Wang and Wu (2006) also concluded that the horizontal motion arises from an area of high viscosity toward regions of low viscosity if the center of deglaciation is situated over a gradient of lateral viscosity change.

By considering the 3D structure in the lithosphere and a homogenous mantle, Yuan and Zhong (2025) show that GIA can cause relative and shear motion between the mantle and lithosphere. During deglaciation, the GIA-induced mantle flow converges toward the former ice sheet center with a larger horizontal velocity than the lithosphere, which tends to have a more coherent direction. During deglaciation, reduced ice loads drive the underlying mantle to flow inward, causing converging surface deformation. In contrast, during the glaciation, the opposite occurs. By examining the time evolution of the horizontal motion induced by idealized ice change, Hermans et al. (2018) found horizontal velocities point inward directly after deglaciation but start to point outward after a time controlled by mantle viscosity. This indicates a diagnostic reversal in the horizontal velocity directions after deglaciation.

We therefore expect that horizontal crustal motions during GIA depend on shallow Earth structure and that the patterns of glaciation-induced mantle flow are controlled by lithospheric flexure and mantle viscosity. Yet, questions remain as to why the vertical and horizontal motions exhibit different degrees of sensitivity to the shallow structure, how the viscoelastic Earth relaxes horizontally during and after deglaciation, and what key factors control the strength and the direction of the surface horizontal motion for more realistic Earth structure. To answer these questions, and to contribute to future coupled ice evolution-Earth structure models taking full account of the constraints provided by GNSS, we focus on the physical processes that govern the dynamics of glaciation-induced mantle flow and its impact of the surface deformation.

We investigate how lateral viscosity variations impact mantle flow, how viscous mantle drag interacts with the elastic response of the lithosphere, and how this viscoelastic system affects the temporal and spatial evolution of horizontal motion. Such efforts are timely, as growing GNSS constraints can be utilized to refine both ice and Earth structure models, in particular since the role of lateral viscosity variations on relatively short wavelength (∼100 km) is crucial for regional relaxation phenomena, including in terms of their effects on ice sheet stability (e.g., Barletta et al., 2018; Book et al., 2022; Gomez et al., 2010, 2018; van Calcar et al., 2025).

2. Methods

We use a numerical, finite-element method for computing the response of a self-gravitating, compressible, rotational Earth with 3D viscoelastic mantle structure to a spatial-temporal varied surface loading forcing as implemented in CitcomSVE-3.0 (Yuan et al., 2025; Zhong et al., 2022). We solve the governing equations for load-induced deformation that are derived from the conservation of mass and momentum and Newton's law of gravitation, applying viscoelastic constitutive equations (Wahr & Zhong, 2013; Wu & Peltier, 1982). The sea level equation with ocean-continent margin evolution is included and incorporates the effects of polar wander and apparent center of mass motion (Mitrovica et al., 2005; Zhong et al., 2003, 2022). For a few test cases, we also use a semi-analytic method for a 1D, spherically symmetric Earth (Wahr and Zhong, 2013), against which CitcomSVE has been benchmarked (Kang et al., 2022; Yuan et al., 2025). For the ice loading history, we use the ICE-6G_C model (Peltier et al., 2015) over the last glacial cycle, beginning at 122 ka, for reference, with the last glacial maximum (LGM) at 26 ka and substantial deglaciation of the North American and Fennoscandian ice sheets completed by ∼7 ka (Peltier et al., 2015).

Table 1
Rheological Parameters Used for All Models Discussed

	Lithosphere (Pa s)	Upper mantle (Pa s)	Lower mantle (Pa s)	LVV
VM5a	10^{26} (0–60 km)	4.8×10^{20} (100–670 km)	1.5×10^{21} (670–1,170 km)	No
	10^{22} (60–100 km)		3.0×10^{21} (1,170 km-CMB)	
1D_REF	10^{26} (0–100 km)	VM5a	VM5a	No
3D_T_e	10^{26} (T_e)	VM5a	VM5a	No
3D_T_e_LVVs(TX19)	10^{26} (T_e)	VM5a	VM5a	TX19
3D_T_e_LVVs(REVEAL)	10^{26} (T_e)	VM5a	VM5a	REVEAL
3D_T_e_LVVs(TX19)_stiffer LM	10^{26} (T_e)	VM5a	3.0×10^{22} (670 km-CMB)	
3D_noT_e_LVVs(TX19)	no	VM5a	VM5a	TX19
3D_$T_{e,2layers}$_LVVs(TX19)	10^{26} (0–60 km in T_e)	VM5a	VM5a	TX19
	10^{22} (60–100 km in T_e)			
3D_$T_{e,97km}$_LVVs(TX19)	10^{26} (T_e with global average of 97 km)	VM5a	VM5a	TX19
3D_$T_{e,e30}$_LVVs(TX19)	10^{30} (T_e)	VM5a	VM5a	TX19
3D_T_e_LVVs(TX19) WeakZone	10^{26} (T_e)	VM5a	VM5a	TX19_LVZ
3D_T_e_LVVs(TX19) ContRoot	10^{26} (T_e)	VM5a	VM5a	TX19_CR

We assume an Earth structure consisting of a Maxwell viscoelastic mantle overlain by a high viscosity lithosphere. In classical flexure studies, elastic thickness, T_e, is defined for a purely elastic plate overlying an inviscid half-space under long-term loading on timescales of millions of years (Watts, 2001). Following other GIA studies, we treat the lithospheric T_e as a layer with sufficiently high viscosity with 10^{26} Pa s to behave effectively as a purely elastic plate over GIA timescales. In 1D models the elastic and viscoelastic properties of Earth's interior are assumed to be spherically symmetric, with density and elastic structure defined solely as a function of depth and taken from PREM (Dziewonski & Anderson, 1981). For 1D viscosity, the widely used VM5a model is characterized by five layers from the surface to core mantle boundary (CMB) (Table 1; Peltier et al., 2015). The VM5a model consists of a 60 km thick, high-viscosity lithospheric layer underlain by a 40 km thick sub-lithospheric layer with viscosity of 10^{22} Pa s. We build our 1D reference model (1D_REF) using the same upper and lower mantle viscosity structure as VM5a, while adopting a uniform lithospheric thickness of 100 km. This value is close to the regional average of the laterally varying T_e used in our 3D model. We also run models with an additional sub-lithosphere layer as comparison.

Our 3D structure models consist of variable T_e in the lithosphere and lateral viscosity variations in the mantle. We use the mean lithosphere thickness model from Steinberger and Becker (2018), which is an average of five estimates determined from different seismic tomography models. These shear wave speed based estimates are meant to define the depth to which the mantle is rheologically strong; those depths are well-correlated with elastic thickness, while typically a factor ∼two larger (Steinberger & Becker, 2018). We thus scale the lithospheric thickness model with a factor of 0.47 resulting in a global average thickness of 46 km, with regional averages of 84 km in North America and 107 km around Hudson Bay. These values are compatible with the mean value inferred from analysis of global or regional RSL observations (Lambeck et al., 2014; Yousefi et al., 2021) and enable comparison to output from 1D models.

For lateral viscosity variations, we apply two recent, global, shear wave speed seismic tomography models as exemplars, TX19 by Lu et al. (2019) and REVEAL by Thrastarson et al. (2024). TX19 is a hybrid model which accounts for structure in Wadati Benioff zones before global inversion and is based on a large, well-established data set of high-quality body wave measurements. We use it as a more "traditional," longer wavelength model in comparison to REVEAL which is based on full waveform inversion and a more "modern" model with a higher degree of spatial heterogeneity (Figure 2). The RMS and spectral character of these models are quite different in the upper mantle; for example, at 300 km depth, REVEAL has ∼3 times larger RMS variations (∼1.5%) than TX19, and the spherical harmonic power per degree and unit area decays with degree, l, approximately as $\propto l^{-1.6}$ between $4 < l < 21$ whereas TX19 is ∼twice as smooth in the sense of showing roughly $\propto l^{-3}$ decay in that range.

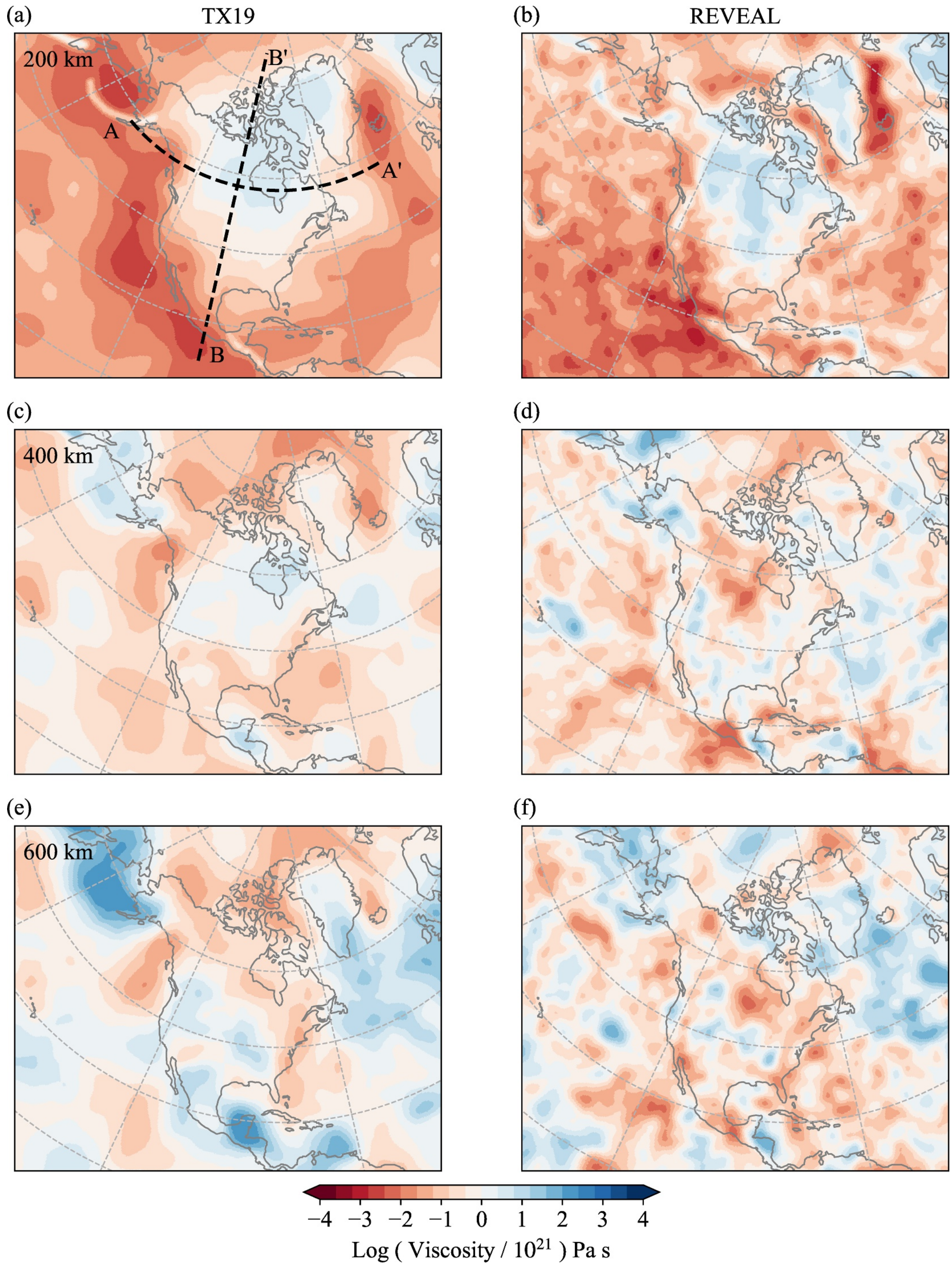

Figure 2. Lateral viscosity variations at depths of 200 km, 400 and 600 km derived from two global seismic shear wave tomography models, TX19 and REVEAL. Profiles A-A′ and B-B′ indicate the cross sections shown in subsequent figures. A Lambert Conformal Conic Projection is used here and in all following map view figures.

Variations in seismic wave velocity reflect differences in the mantle's thermal and/or compositional structure. The mapping between velocity and density or viscosity anomalies is thus complex and affected by mineral physics and chemical heterogeneity. However, for simplicity, we assume that temperature is the dominant controlling factor. In an approach similar to mantle circulation computations (e.g., Becker, 2006), we follow Latychev et al. (2005) to infer viscosity using:

$$\delta \ln \rho(r,\theta,\varphi) = \frac{\partial \ln \rho}{\partial \ln v_s}(r)\delta \ln v_s(r,\theta,\varphi) \tag{1}$$

$$\delta T(r,\theta,\varphi) = -\frac{1}{\alpha(r)}\delta \ln \rho(r,\theta,\varphi) \tag{2}$$

$$\eta(r,\theta,\varphi) = \eta_0 e^{-\epsilon \delta T(r,\theta,\varphi)} \tag{3}$$

where r, θ, and φ are the radius, colatitude, and longitude, respectively. The term $\delta \ln v_s(r,\theta,\varphi)$represents seismic shear wave velocity anomalies and $\frac{\partial \ln \rho}{\partial \ln v_s}(r)$ is a depth-dependent scaling factor used to convert the velocity perturbations to density variations (Equation 1). Following Yousefi et al. (2021), we use the radial profile of Forte and Woodward (1997) for the scaling factor with a range of ∼0.1–0.35, to convert velocity to density anomalies (Equation 1). Temperature anomalies are then calculated by scaling the density anomaly field using the radially variable coefficient of thermal expansion ($\alpha(r)$ in Equation 2) in Chopelas and Boehler (1992). The 3D viscosity structure $\eta(r,\theta,\varphi)$ is constructed by perturbing the reference viscosity (η_0) in 1D_REF, using an approximate temperature dependent viscosity with a scaling factor, ϵ, that determines the degree of dependence of the viscosity structure on temperature. We set this parameter to 0.035°C^{-1} for TX19 and 0.017°C^{-1} for REVEAL, to account for the tomography model RMS differences, such that this scaling yields comparable viscosity variations spanning five to six orders of magnitude for both models. The constructed 3D viscosity model has the same global average as the reference 1D model by design but differs in terms of the regional averages (e.g., in North America). This can introduce biases when comparing predictions from the 1D and 3D GIA models; to minimize such 1D model dependent bias, we further adjust the 3D viscosity so that its regional average over North America matches that of the reference model in 1D_REF (Figure 3). All input fields in 3D GIA models, including the ice model, variable T_e, and lateral viscosity variations were interpolated on the finite element surface grids with lateral resolution of ∼25 km by 25 km. The radial finite-element node-distance is 5 km for the upper 420 km depth, 10 km between 420 and 670 km and 40–60 km between 670 and the CMB.

We show the lateral viscosity variations at depths of 200, 400, and 600 km for TX19 and REVEAL in Figure 2, and depth cross sections from the surface to CMB along two profiles (i.e., an east-to-west profile A-A′ at latitude 57°N and a north-south profile B-B′ at longitude 260°), as well as depth profiles of the regional-averaged viscosity variations in Figure 3, using a geometric average. While both 3D viscosity models capture the main tectonic features, for example, stiff continental cratons and weak oceanic asthenosphere, the inferred viscosity structure differs in detail. For example, TX19 shows relatively smooth gradients in viscosity, with fast (i.e., strong) material, perhaps craton plus slab (cf. Porritt et al., 2021) extending to ∼500 km depth. In contrast, the REVEAL based model shows more short-wavelength variations and a slightly stiffer but shallower continental root beneath Hudson Bay, reaching ∼300–400 km depth (Figures 2 and 3). The weak asthenosphere in the TX19 model is more extensive and continuous (Figures 2a and 2c), while the REVEAL model produces more localized gradients in the oceanic asthenosphere, with more clearly delineated, long and narrow high-viscosity (cold) anomalies (e.g., the Cascadia slab, cf. Hua et al., 2025; Figures 2b and 2d).

The radial profiles for each 3D model, including the global and regional means over North America and Hudson Bay are shown in Figure 3e. The 3D variable elastic thickness model we use has an average elastic lithosphere thickness of ∼100 km beneath Hudson Bay (colored dotted curves). Regionally averaged profiles beneath North America (colored dashed curves) show a gradual decrease in viscosity from 10^{26} Pa s near the surface to 5×10^{20} Pa s at the lithosphere-asthenosphere boundary, reflecting the influence of the weak oceanic asthenosphere surrounding the continental plate. The global average T_e model (colored solid curves) shows a relatively sharper decrease in viscosity at shallow depths, consistent with a global weak asthenosphere. The profiles also confirm that our 3D lateral viscosity variations in the mantle have a regional average over North America that is consistent with the reference viscosity in 1D_REF. The viscosity parameters for all models discussed are summarized in Table 1.

3. Results

We present our results for surface motion and mantle flow during and after deglaciation, but the calculation starts at the end of the last interglacial (∼122 ka) to capture the non-equilibrium state induced by ice accumulation prior

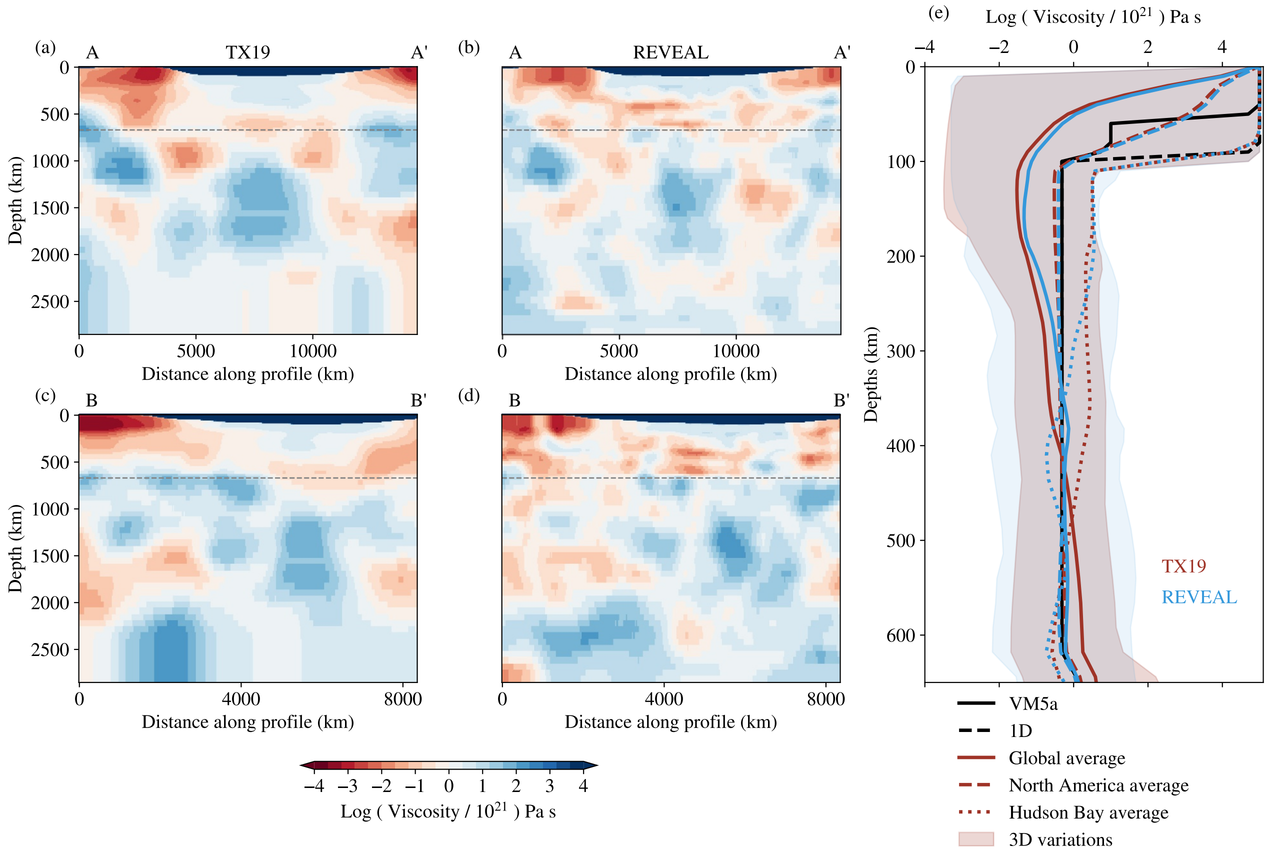

Figure 3. Cross sections of lateral viscosity variations based on TX19 and REVEAL tomography along profiles A-A′ and B-B′ (a–d), extending from the surface to the core-mantle boundary (CMB). The gray dashed line marks the 670 km interface between the upper and lower mantle. Panel (e) shows the depth-dependent viscosity profiles for VM5a (black solid line), 1D_REF (black dashed line), and depth-averaged viscosities from TX19 (red) and REVEAL (blue) averaged over Hudson Bay (dotted), North America (dashed), and globally (solid). The shaded region denotes the range of viscosity variations in the 3D models.

to the LGM. We also extend our predictions of surface and mantle motion 10 ky into the future to investigate the relaxation of horizontal motions with and without heterogeneity structures to get a more complete understanding of the physical processes.

3.1. Surface Motion for 1D Viscosity

We vary the elastic thickness of the lithosphere between 46, 100 and 146 km, the upper-mantle viscosity as 0.2 and 1×10^{21} Pa s and the lower-mantle viscosity as 1 and 10×10^{21} Pa s. Figure 4 shows the time evolution of the surface vertical velocity and the horizontal divergence,

$$\mathrm{div}_H(\theta_i, \varphi_i) = \left(\frac{1}{r}\sin\theta\right)\partial(\sin\theta v_\theta)\partial\theta + \left(\frac{1}{r}\sin\theta\right)\partial(v_\varphi)\partial\varphi,$$

where v_θ and v_φ are the velocities in colatitude and longitude, and r, θ, φ the radius, co-latitude and longitude, averaged around Hudson Bay

$$\mathrm{div}_{H\_ave} = \frac{\sum_{i,j}\mathrm{div}_H(\theta_i, \varphi_i)\sin\theta_i\Delta\theta\Delta\varphi}{\sum_{i,j}\sin\theta_i\Delta\theta\Delta\varphi} \tag{4}$$

(red frame in Figure 1), together with the total ice volume change and rate of change in North America from 30 ka to the present-day. The rate of ice change was calculated from the incremental ice mass at each timestep, consistent with the loading formulation used in GIA modeling.

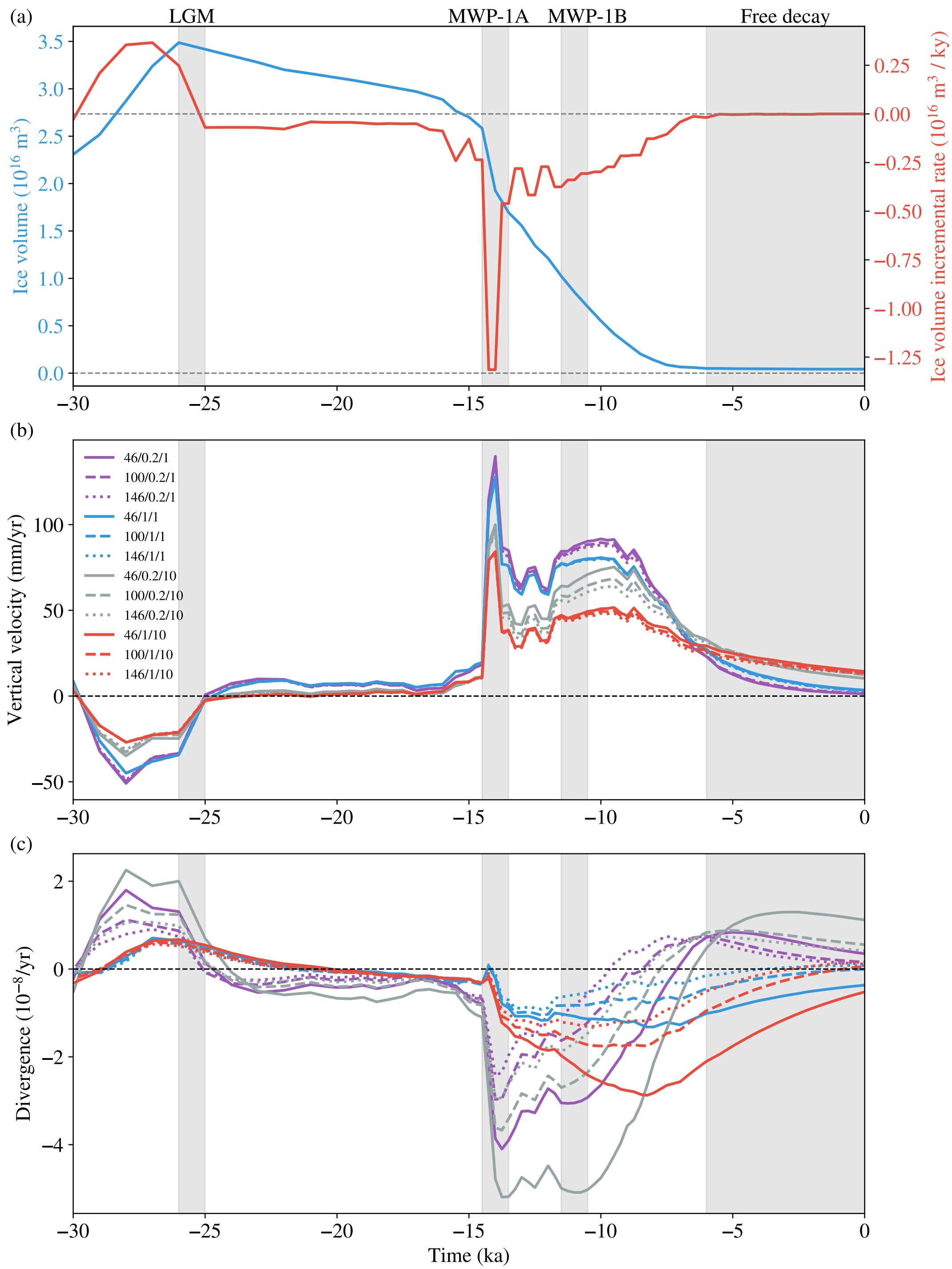

Figure 4. Time evolution of ice change, vertical velocity and horizontal divergence from 1D models. (a) Total ice volume over North America for ICE-6G_C (blue) and its rate of change (red), computed from the incremental ice volume at each timestep, consistent with the loading formulation used in GIA modeling. (b) and (c) Regional mean surface vertical velocities and horizontal divergence over North America from 1D models with varying lithosphere thickness (46 km, 100 km, 146 km), upper mantle viscosities (0.2 and 1 $\times 10^{21}$ Pa s) and lower mantle viscosities (1 and 10 $\times 10^{21}$ Pa s). The legend denotes parameter combinations such as T_e/upper mantle viscosity/lower mantle viscosity. Colors represent different viscosity pairs, and line type indicate lithosphere thickness. The shaded regions indicate the time periods for LGM (~26 ka), MWP-1A (~14 ka), MWP-1B (~11 ka), and free decay period (<7 ka).

We find a negative correlation between vertical velocity and horizontal divergence throughout the glaciation history. Increases in ice mass drive surface subsidence accompanied by outward horizontal motion, whereas decreases in ice mass produce uplift and horizontal convergence, consistent with Yuan and Zhong (2025), for example, In addition, our results reveal that the timing of these mode transitions (e.g., from subsidence to uplift vertically and from divergence to convergence horizontally) differs between vertical and horizontal components. Vertical motion shows an in-phase response to ice mass change: as ice mass begins to decrease, vertical velocity switches from negative to positive. By contrast, the horizontal motion shows hysteresis and out-of-phase response, and the timing of the transition in horizontal motion is sensitive to upper mantle viscosity. For example, in the weak upper mantle case (0.2×10^{21} Pas), the transition starts earlier (∼24 ka), whereas in the strong upper mantle case (10^{21} Pas), convergence is delayed until ∼20 ka.

The results indicate the viscous mantle deformation has a delayed horizontal response to the ice mass variation, which is strongly dependent on shallow mantle viscosity. During the postglacial period (e.g., decreasing surface ice loading), while the verticals continue to uplift with mantle stress relaxation beneath the ice center, the horizontals exhibit potential reversal in the directions. The timing of the reversal and the peak horizontal motion rate is mainly controlled by upper mantle viscosity. For example, Figure 4 shows a reversal around 8 ka with a larger peak rate in the cases with 0.2×10^{21} Pas upper mantle viscosity, whereas cases with 10^{21} Pas show no reversal until the present day and a small peak rate. Lithospheric thickness and lower mantle viscosity will further modulate the timing of the reversal and the peak rate. For a given lower mantle viscosity, a thicker lithosphere leads to an earlier reversal with a smaller peak rate (e.g., dotted vs. solid purple curve). For a fixed elastic lithosphere thickness, the transition starts earlier for a weaker lower mantle with smaller peak rate (e.g., solid curve in purple compared with the one in gray). Distinct evolutionary paths arising from different viscosity combinations can converge to similar horizontal divergence values at present-day, indicating that those parameters play a minor role for interpretation of present-day geodetic observations. Positive present-day divergence can follow an early reversal with decaying amplitude toward the present (e.g., softer upper mantle), or a late reversal with slightly increasing amplitude toward the present (e.g., stiffer upper mantle with a relatively thick lithosphere). Models with a slower reversal process predict convergent (negative) divergence at present-day (e.g., stiffer upper mantle with a relatively thin lithosphere).

3.2. Surface Motion for 3D Viscosity

We calculated the present-day surface vertical and horizontal motion for two 1D models with VM5a and 1D_REF, together with three 3D models including variable elastic lithosphere thickness ("3D_T_e") and two lateral viscosity variation (LVV) structures ("3D_T_e_LVVs(TX19)" and "3D_T_e_LVVs(REVEAL)"). Figure 5 compares the predicted vertical and horizontal velocities and dilatations among these models. We also examine the correlation between vertical velocities and horizontal dilatation, where such relationships have been suggested as a means to disentangle edge-driven tectonic uplift due to far field forcing versus deep source driven vertical motions associated with mantle convection (e.g., Faccenna et al., 2014), with complications in the GIA context (e.g., Lau et al., 2020).

The 1D_REF model predicts outward horizontal motion around the rebound center with a larger amplitude, indicating stronger extensional deformation around Hudson Bay (Figures 5b and 5g), compared to the VM5a case (Figures 5a and 5f). Incorporating variable elastic lithosphere thickness leads to convergent horizontal motions in areas of thinner lithosphere (e.g., the Pacific coastline and the southern U.S.; Figure 5c), and results in a pronounced negative dilatation along the West Coast (Figure 5h), a feature not observed in the 1D cases. Including lateral viscosity variations in the 3D_T_e case further changes the motion patterns, with an overall northern horizontal motion for both 3D_T_e_LVVs(TX19) and 3D_T_e_LVVs(REVEAL) (Figures 5d and 5e). Compared with a homogenous mantle, adding LVVs causes smaller wavelength variations in dilatations, with compressional deformation around Hudson Bay (Figures 5i and 5j). The strong compressional zone along the West Coast in 3D_T_e disappears when LVVs are included, as the weak asthenosphere beneath the oceanic lithosphere promotes a faster mantle relaxation and hence a smaller residual in lithospheric stress and deformation at the present day (Figures 5i and 5j vs 5h). The impact of LVVs on surface motion is evident in the correlation map (Figures 5k–5o). While the 1D viscosity models show an overall positive correlation between uplift and divergence, the cases incorporating LVVs show localized negative correlations around Hudson Bay, indicating that uplift in the crust is accompanied by compressional horizontal deformation (Figures 5n and 5o).

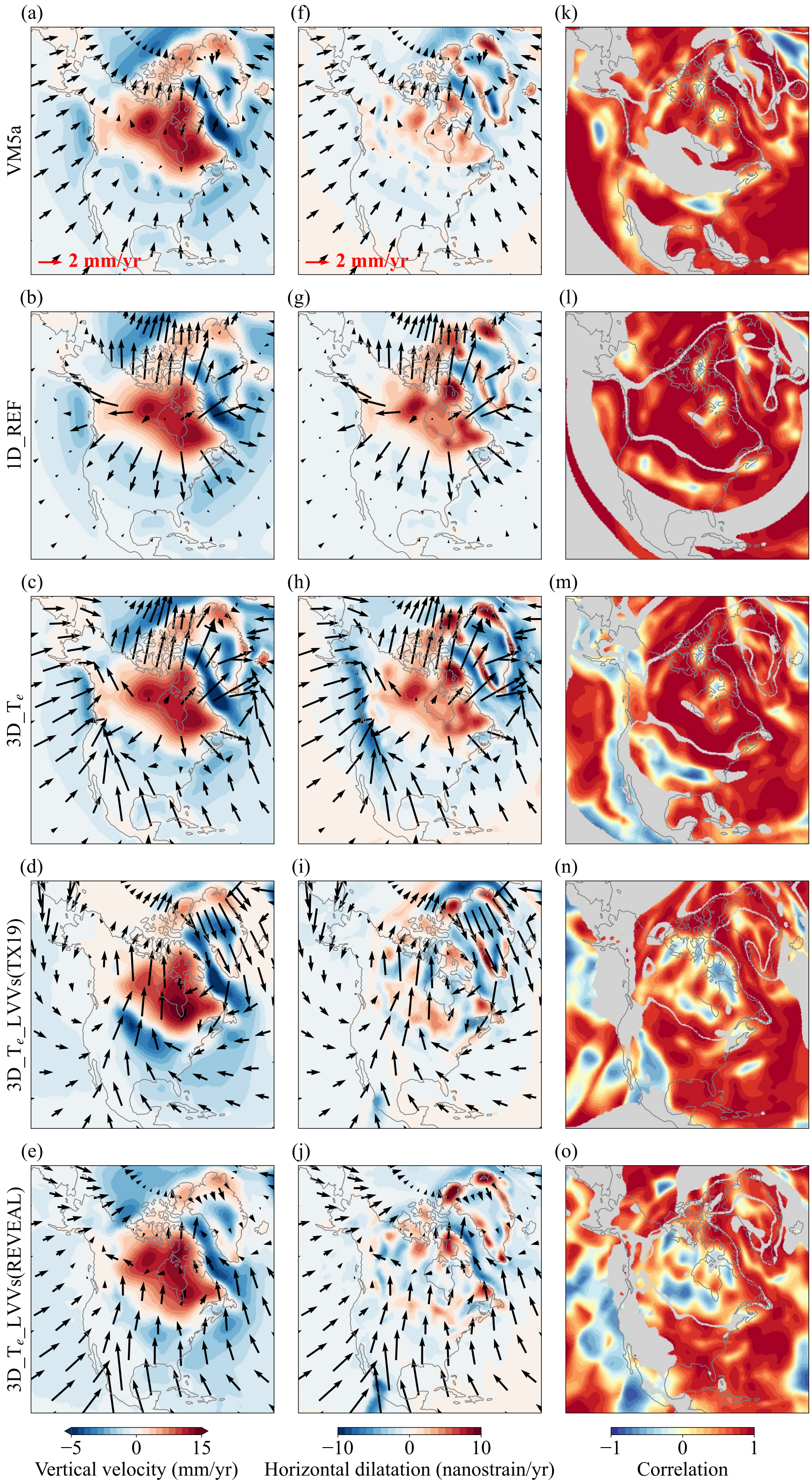
(a)
(f)
(k)
VM5a
2 mm/yr
2 mm/yr
(b)
(g)
(l)
1D_REF
(c)
(h)
(m)
3D_T$_e$
(d)
(i)
(n)
3D_T$_e$_LVVs(TX19)
(e)
(j)
(o)
3D_T$_e$_LVVs(REVEAL)
−5
0
15
Vertical velocity (mm/yr)
−10
0
10
Horizontal dilatation (nanostrain/yr)
−1
0
1
Correlation

Figure 5.

To investigate the time evolution of surface motions we also calculate the regionally averaged vertical velocity and horizontal divergence around Hudson Bay from 30 ka to 10 ky into the future. The vertical velocity shows similar evolution for 1D and 3D cases, which are highly correlated with the rate of ice change (Figure 6a). The horizontals show a range of divergence trajectories, with greatest spread during the fast ice melting and the postglacial free decay periods. While the mode transition during the LGM occurs at approximately the same time, the timing of the postglacial reversal varies substantially among the cases. All three homogenous mantle models (e.g., VM5a, 1D_REF, 3D_T_e) predict a postglacial reversal during the mid-Holocene, with the reversal timing differing by 2–3 ky (Figure 6b). Adding lateral variations in mantle viscosity (e.g., 3D_T_e_LVVs(TX19) and 3D_T_e_LVVs (REVEAL)) delays the postglacial reversal, showing negative dilatation through the present followed by a slight positive dilatation from the present to the future, indicating the transition occurs around the present day.

The spatial evolution of horizontal velocities and dilatation for the 1D and 3D cases from 8 ka to 10 ky in the future is shown in Figure 7. The two homogeneous 1D models exhibit similar spatial evolution of the dilatation field but differ in both timescale and amplitude. By 8 ka, after most of the ice melting occurred, Hudson Bay undergoes compressional deformation, surrounded by a peripheral belt of mild extension, along with convergent flow toward Hudson Bay. As viscous relaxation proceeds, the zone of extension gradually broadens outward from Hudson Bay, while the central compression weakens over time and eventually transitions to extension. The horizontal motion also evolves from convergence to divergence. This extension continues over the entire former ice-covered region beyond the present day and diminishes by ∼10 kyr in the future. The VM5a case shows a delayed transition and smaller horizontal velocities compared with 1D_REF, consistent with the time evolution curves in Figure 6.

With variable lithosphere thickness (3D_T_e), the region within the western North American Cordillera shows strong compression. Variable T_e adds complexities in the elastic flexure strength, with thin (∼10–40 km) lithosphere along the western North American and thick (∼50–120 km) over the Canadian craton, which can contribute to the extended, narrow zone of compression deformation across the West Coast. In the variable T_e model, horizontal motion beyond the south of the Laurentide ice sheet margin is directed toward the former ice center, consistent with the VM5a model but opposite to the 1D_REF case, which predicts motion directed away from the ice center. Within the Laurentide Ice Sheet, the horizontal velocity and the deformation pattern for 3D_T_e are largely consistent with the 1D_REF case. The region-dependent similarity in horizontal motion between 3D_Te, 1D_REF, and VM5a indicates that these models share comparable lithospheric thickness structures in those regions.

With lateral viscosity variations included in 3D_T_e_LVVs(TX19) and 3D_T_e_LVVs(REVEAL), the deformation field shows more pronounced short-wavelength features, characterized by alternating zones of compression and extension across the former ice-covered region. In both cases, Hudson Bay remains in compression up to the present day, and the deformation gradually transitions to extension beyond the present and persists into the future. This behavior is consistent with the time evolution curves shown in Figure 6. Compressional deformation along the West Coast which developed during the postglacial period in the 3D_T_e case was not observed when LVVs included, indicating the tradeoff between the thin lithosphere and the low viscosity zone beneath this region. For 3D_T_e_LVVs(TX19), a strong southward motion over the LGM ice cover is observed from 14 to 8 ka, followed by a reversal to northward motion. The REVEAL case shows continuous northward motion from 14 ka to the present, with only minor localized directional changes. Around the southwest of Hudson Bay, the TX19 case predicts positive present-day divergence while the REVEAL case predicts negative divergence (0 ka, Figure 7), which may be attributed to the low viscosity anomaly at 400–600 km depth in the REVEAL model (Figure 3d). Furthermore, the REVEAL case shows the largest present-day horizontal velocities, accompanied by a narrow zone of negative divergence near the southern Mexican border along the West Coast (0 ka, Figure 7), coinciding with the region of lowest viscosity at 400 km depth in REVEAL (Figure 3d). These results demonstrate that small-scale viscosity anomalies in the middle to deep upper mantle can influence surface horizontal velocity patterns, even in the far field.

Figure 5. Present-day surface motions, dilatation, and correlation maps. Panels (a)–(e) show vertical and horizontal velocity fields for VM5a, 1D reference model (1D_REF), 3D model with variable lithosphere thickness (3D_T_e), and lateral viscosity variations from TX19 (3D_T_e_LVVs(TX19)) and REVEAL (3D_T_e_LVVs (REVEAL)). Panels (f)–(j) show horizontal dilatations for each model overlain by horizontal velocity vectors. Panels (k)–(o) show correlation maps between vertical velocity and horizontal dilatation, computed by sampling fields within a moving spherical cap with 500 km radius. Gray, masked out regions denote areas where either vertical or horizontal velocity magnitude is <0.4 mm/yr.

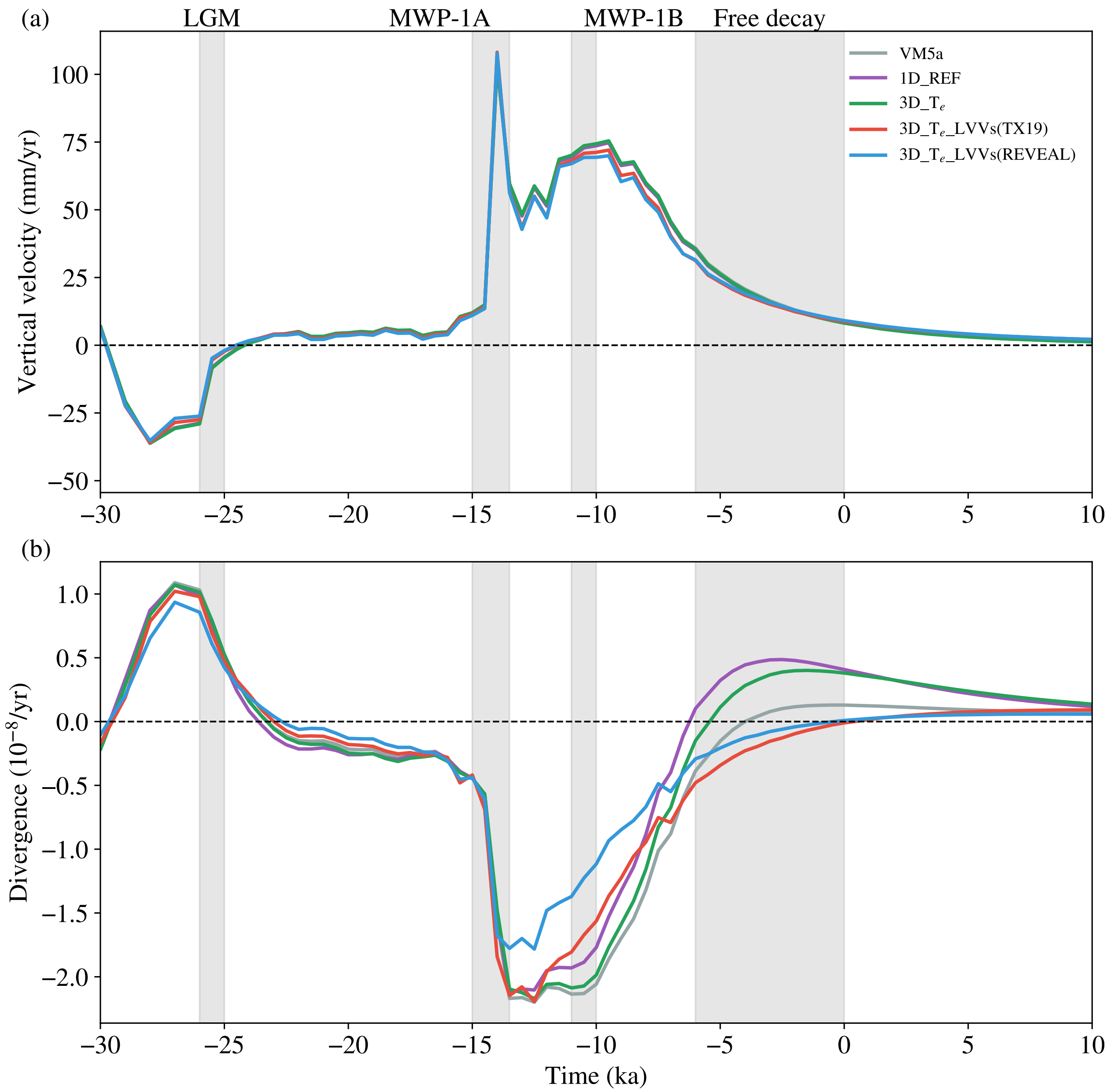

Figure 6. Time evolution of the regional average surface vertical velocity (a) and horizontal divergence (b) over North America for VM5a, 1D_REF, and 3D models with variable lithosphere thickness (3D_T$_e$), and lateral viscosity variations from TX19 (3D_T$_e$_LVVs(TX19)) and REVEAL (3D_T$_e$_LVVs(REVEAL)). The shaded regions are the same as in Figure 3. The region used for the averaging is shown as the red box in Figure 1.

3.3. Mantle Return Flow After the Last Deglaciation

Surface loading generally drives mantle flow away from the load region during loading and back toward it during unloading (e.g., mantle return flow). While our 1D and 3D models are broadly consistent with this picture, our calculations also indicate additional complexities arising from horizontal variations in the lithosphere and mantle strength. Figures 8 and 9 show present-day velocities along cross-sections beneath North America, with the profile locations indicated in Figure 2. In the 1D_REF case, the deep upper mantle flows upward and inward toward the previously ice loading regions while the shallow upper mantle and lithosphere flow upward and outward (e.g., reversal mantle return flow in the shallow depths), indicating a cell-like flow pattern in addition to vertical motion (Figures 8a and 9a). The lithosphere with variable thickness induces slightly faster circulation flow beneath the thinner lithosphere, while the similar flow patterns remain beneath the craton (Figures 8b and

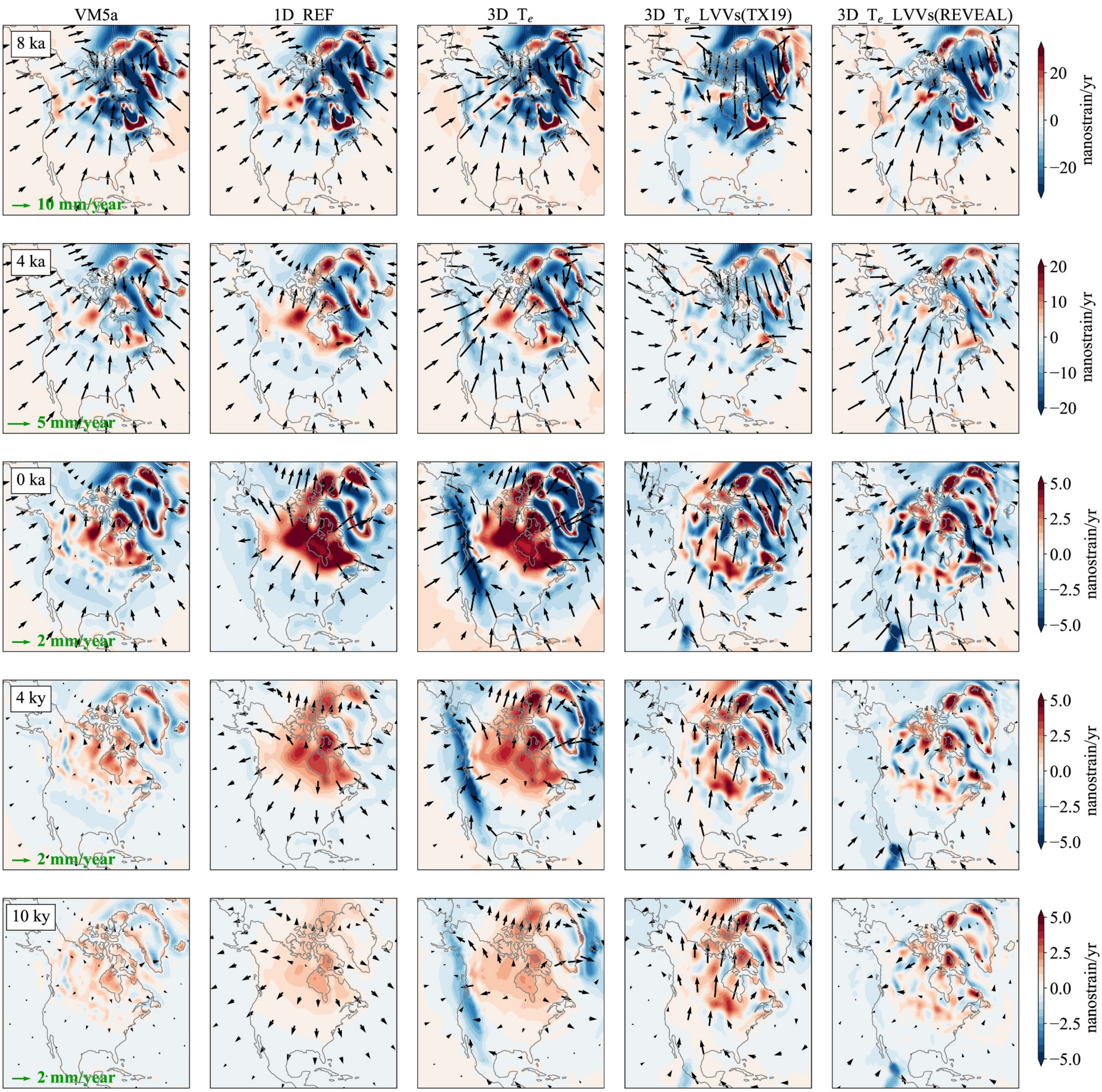

Figure 7. Time evolution of the surface horizontal velocities and dilatations for VM5a, 1D_REF, and 3D models with variable lithosphere thickness (3D_T$_e$), and lateral viscosity variations from TX19 (3D_T$_e$_LVVs(TX19)) and REVEAL (3D_T$_e$_LVVs(REVEAL)). Each row from the top to bottom are maps at 8 ka, 4 ka, present-day and 4 ky and 10 ky in the future.

9b). Note the thinner oceanic lithosphere along the western margin of the craton promotes inward downwelling at shallower depths (~0–100 km depth in Figure 8b), where it converges with the outward upwelling, resulting in the strong compressional zone across the West Coast illustrated in Figures 5 and 7.

The horizontal viscosity contrast between the stiffer root and the weaker oceanic asthenosphere guide upper mantle flow horizontally in the low viscosity zones and vertically in the high viscosity zones, producing a "box-like" flow pattern (Figures 8c and 8d). The strength of the flow is controlled by LVVs, where the broader and weaker viscosity zone together with a deeper continental root in TX19 produces a slightly faster horizontal flow beneath the peripheral bulge along the West Coast and a faster vertical flow beneath the rebound center (Figure 8c), compared with those from REVEAL (Figure 8d). The low viscosity (~10^{17}–10^{18} Pa s) zone within the southwestern North American Cordillera in TX19 generates strong horizontal flow that redirects the circular

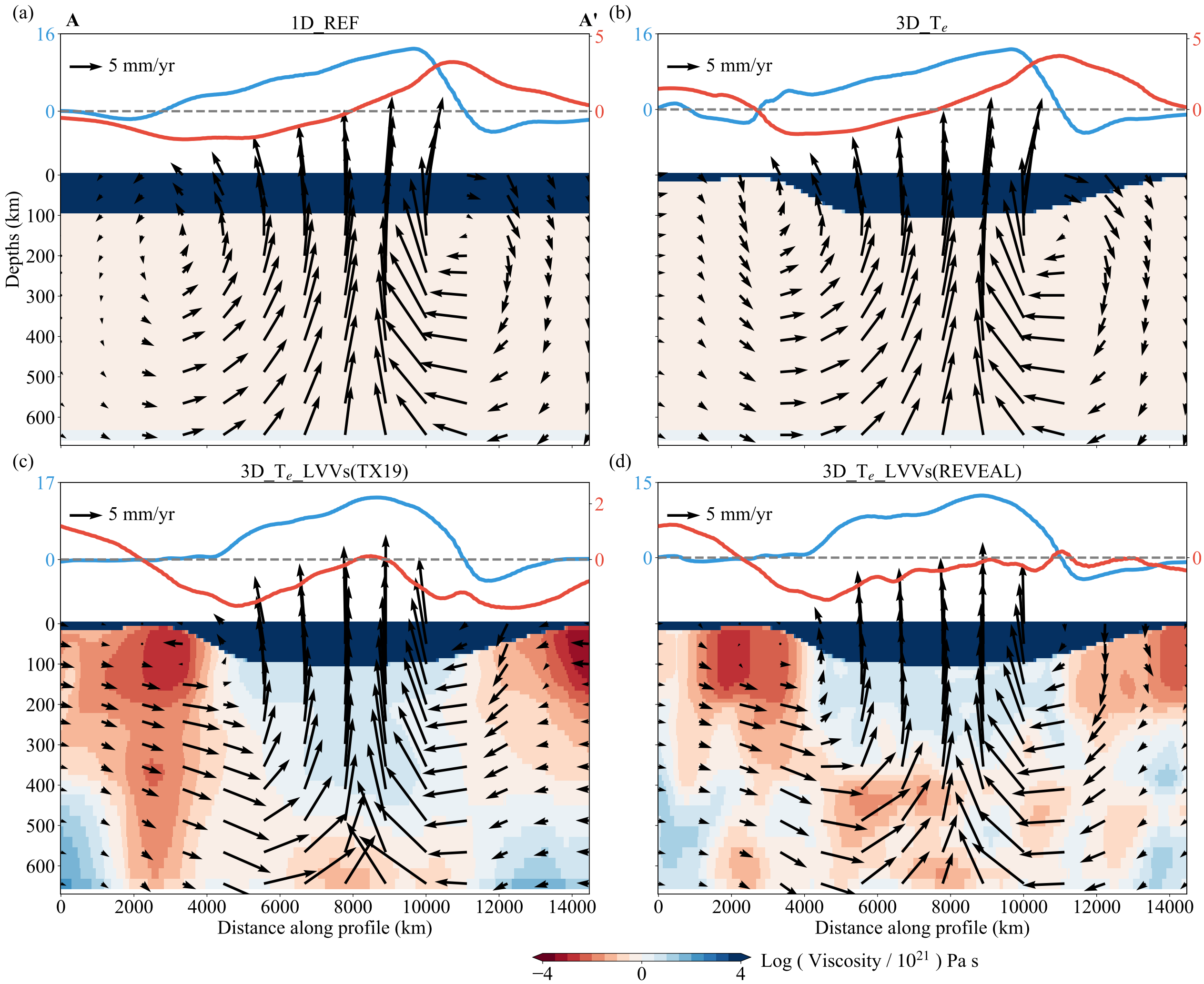

Figure 8. Cross sections for present-day GIA-induced mantle flow velocities along profile A-A′ in Figure 2 for the 1D_REF model, and 3D models with variable lithosphere thickness (3D_T_e), and lateral viscosity variations from TX19 (3D_T_e_LVVs(TX19)) and REVEAL (3D_T_e_LVVs(REVEAL)), extending from the surface to 670 km depth. The colored background indicates viscosity variations, with dark blue denoting the elastic lithosphere. Surface motions along the profile are also shown, with vertical velocities in blue (positive upward) and horizontal velocities in red (positive eastward). The blue (red) number on *y*-axis denotes the amplitude of the vertical (horizontal) velocity scale in mm/yr and differs across panels.

pattern seen for 1D_REF and 3D_T_e into a mainly northward flow beneath North America (Figure 9c), resulting in the persistent northward surface motion in Figure 5d. The REVEAL case predicts a weaker northward flow (Figure 9d), likely due to the zone underneath the Cordillera which is roughly one order of magnitude higher viscosity than that in TX19, and the compensation between short-wavelength high and low viscosity structures (Figures 9c and 9d, also Figures 2 and 3).

The evolution of mantle return flow during deglaciation among 1D and 3D models are shown in Figures 10 and 11. In the homogenous mantle cases (e.g., 1D_REF and 3D_T_e), the mantle flows upward and inward toward the loading center across the western and southern margin of the Laurentide ice sheet during the period of rapid ice retreat and thinning (∼14 ka; Figures 10a, 10d, and 11a, 11d). As the ice retreats to Hudson Bay around 8 ka, the peak surface uplift also migrates to that area, with downward flow beneath the LGM ice margin indicating the peripheral bulge collapse. See, for example, the vertical velocity shifting its peak from 240°W in Figure 10a to 280°W in Figure 10b, and both edges of the curve transition from positive values in Figure 10a to negative in Figure 10b, indicating a change from uplift at 14 ka to subsidence at 8 ka.

Compared with the 1D_REF model, the thinner oceanic lithosphere in 3D_T_e enhances the strength of the regional inward mantle flow at shallower depths, indicating the localized interplay between lithospheric flexure

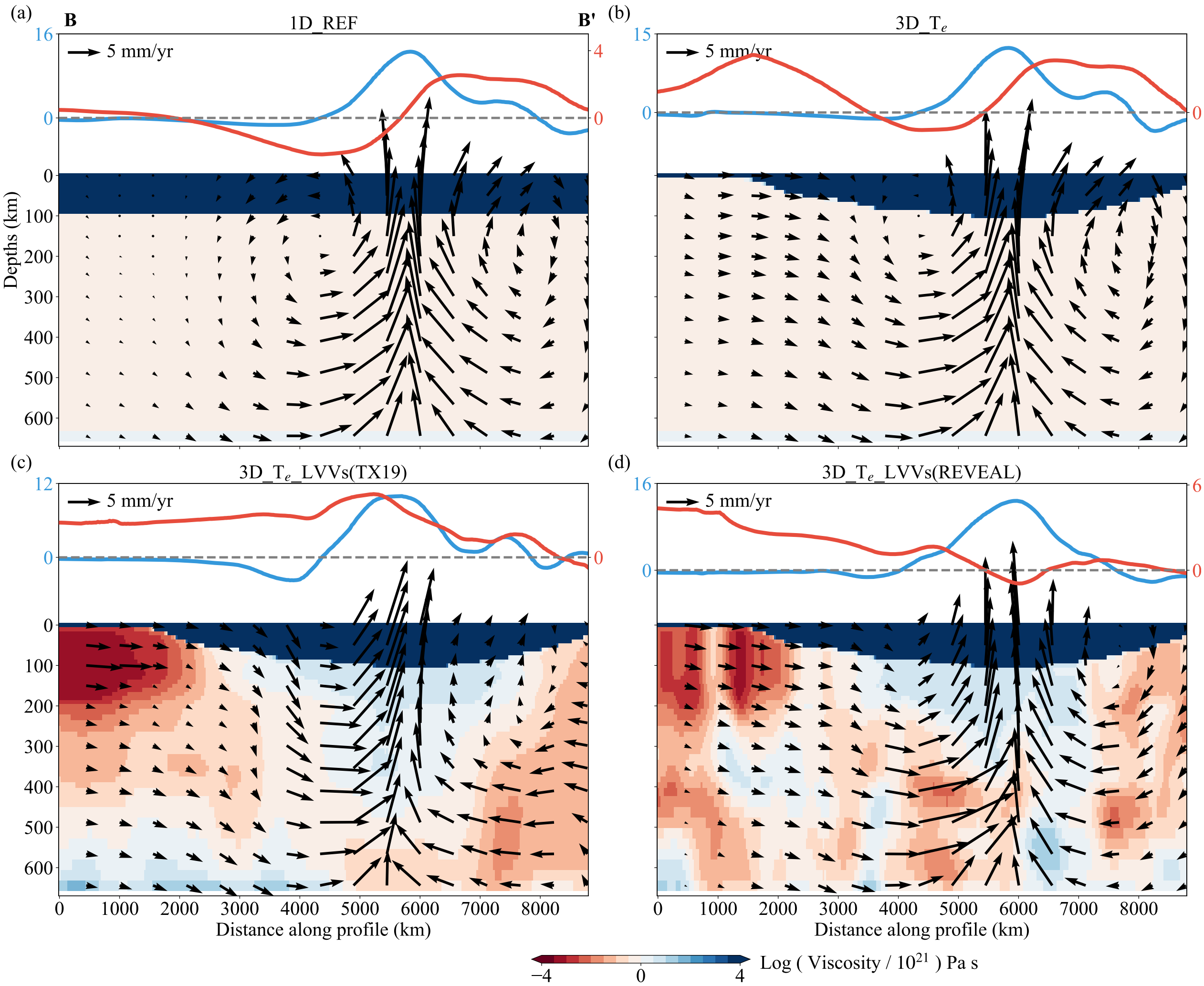

Figure 9. Same as Figure 8, but for cross sections along profiles B-B′ in Figure 2.

and mantle viscous relaxation (Figures 10e and 11e). During the free decay period after the ice entirely disappeared, the upward and inward flow turns into a circular pattern in which the upward and outward shallow upper mantle flow drags the lithosphere (Figures 10c, 10f and 11c, 11f). For example, the horizontal velocity transitions from positive values in Figure 10b to negative in Figure 10c on its left half, indicating a shift from eastward (toward the ice center) at 8 ka to westward motion (away from the ice center) at the present day. The strength of reversal mantle return flow diminishes with increasing distance from the ice margin, transforming to the negligible inward motion in the far field beyond the former ice-covered region in the 1D_REF case. For 3D_T_e, the deglaciation induced inward mantle flow beneath oceanic lithosphere (e.g., 14 ka - 8 ka) decays more slowly during the postglacial period (~8 ka to present), leading to a stronger far field inward flow at shallower depths relative to the 1D_REF model. This enhanced inward flow confines the postglacial reversal in 3D_T_e mainly within and beneath the transition margin between the craton root and the oceanic plate.

LVVs substantially modify the strength and direction of the mantle return flow, and its postglacial reversal timing. The rapid ice retreat and thinning along the western-southern Cordilleran and Laurentide ice sheet margin at 14 ka drives strong horizontal flow within the weak oceanic asthenosphere (e.g., the dashed contours in Figures 10g and 10j), with a slightly downward component, producing subsidence offshore within the Pacific plate. The lateral viscosity contrast also enhances upwellings in the transition region from the weak asthenosphere offshore to the continental root beneath western North America, producing significantly surface uplift inland of Pacific coastline

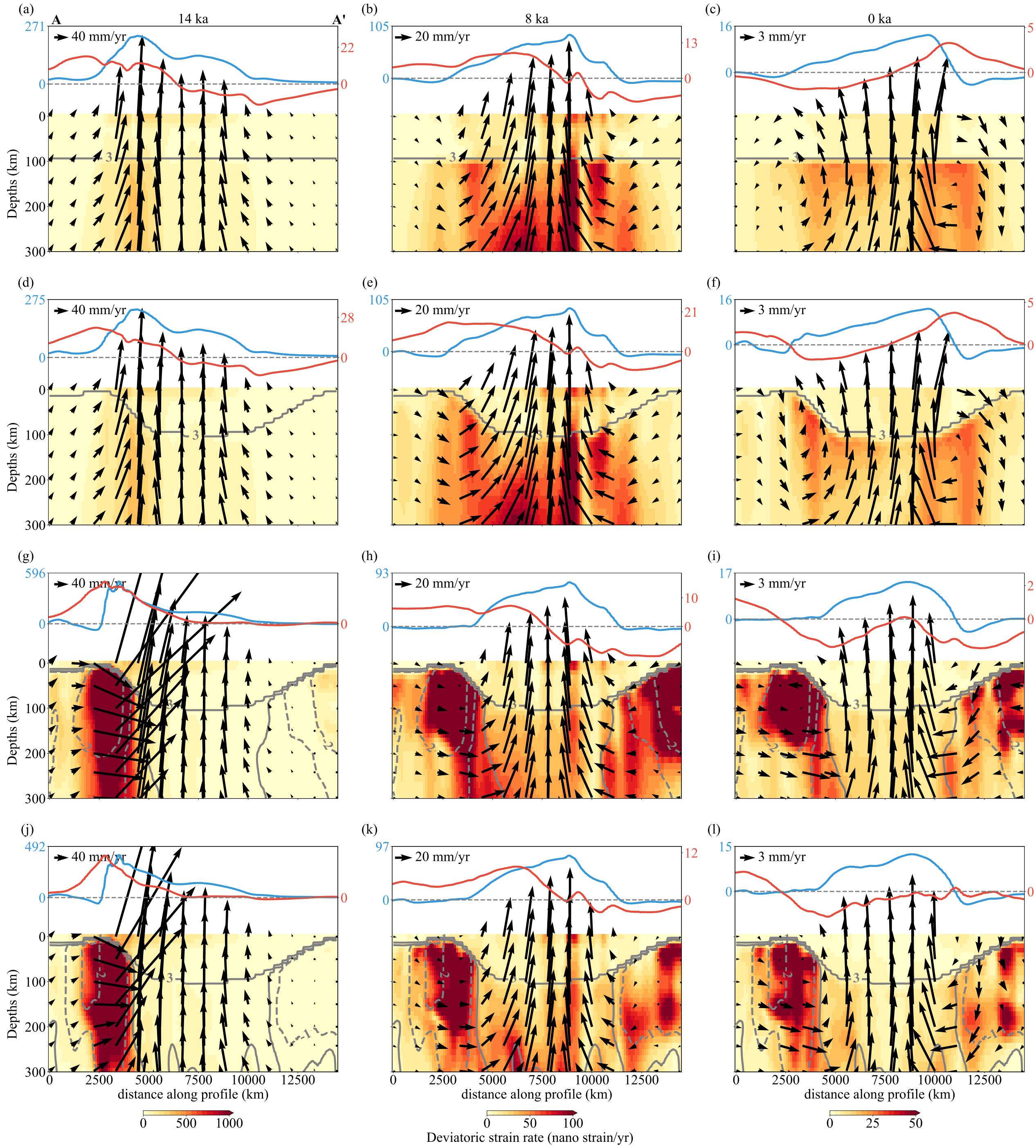

Figure 10. Time evolution of GIA-induced mantle flow velocities along A-A′ cross section in Figure 2, from the surface to 300 km depth. The color map shows the amplitude of the deviatoric strain rate. The contours are viscosity in $\log(\eta/10^{21}$ Pas); with dashed contours indicating the sub oceanic plate weak zone and the solid contours denote the lithosphere and continental root. Blue and red curves represent the vertical and horizontal surface velocities, respectively. The blue (red) number on y-axis denotes the amplitude of the vertical (horizontal) velocity scale in mm/yr and differs across panels. Columns correspond to times at 14 ka, 8 ka and present-day, while rows show different models from the top to the bottom: 1D_REF model, 3D model with variable lithosphere thickness (3D_T_e), and 3D models with lateral viscosity variations from TX19 (3D_T_e_LVVs(TX19)) and REVEAL (3D_T_e_LVVs(REVEAL)).

(Figures 10g and 10j). The peak velocity is ~2 times higher in the vertical direction and ~8 times higher in the horizontal direction than for 1D and 3D_T_e, indicating that the mantle return flow is directed more horizontally in the presence of a weak zone.

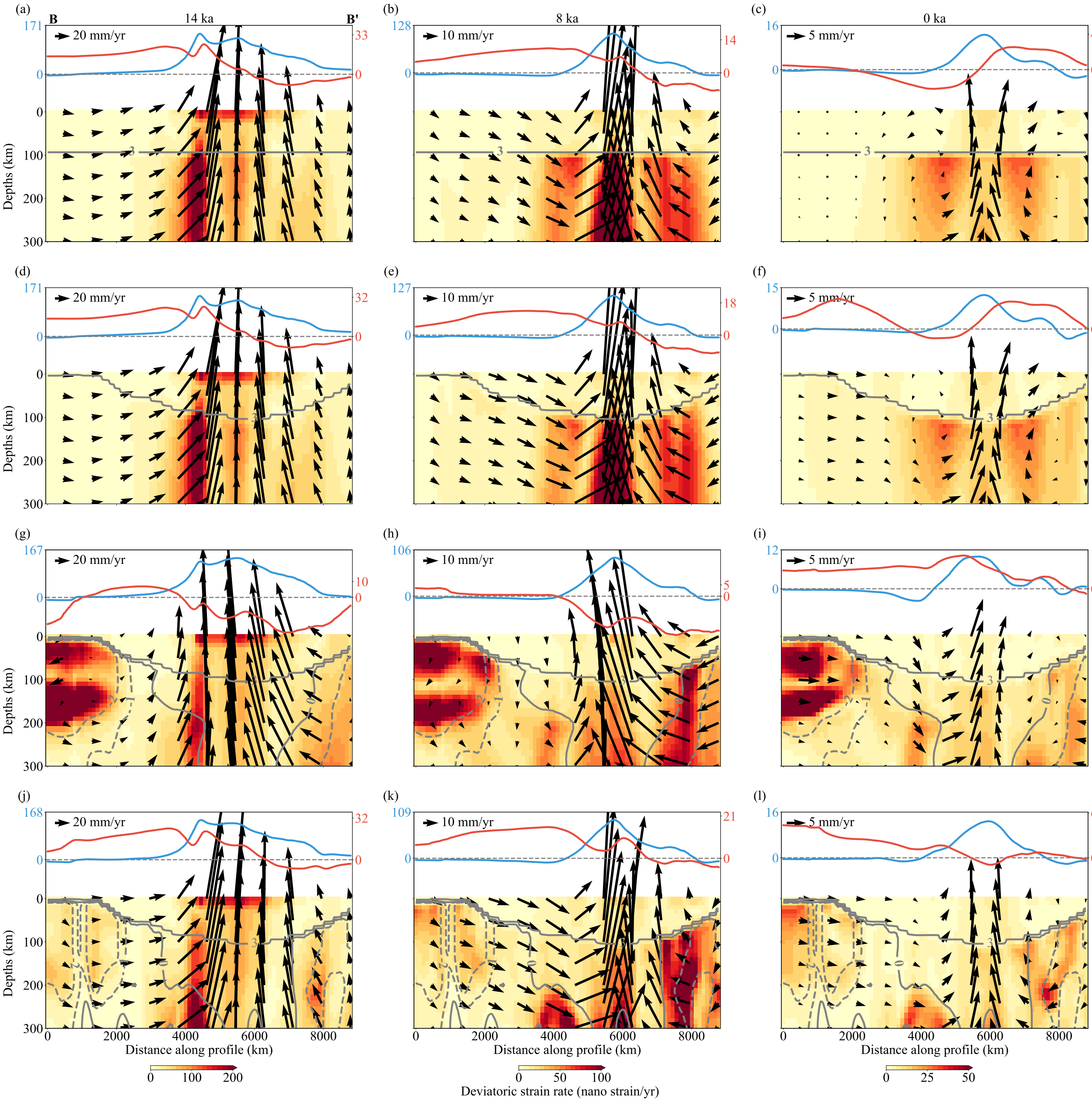

Figure 11. Same as Figure 10, but for B-B′ cross sections in Figure 2.

The horizontal return flow in the shallow upper mantle continues with a diminished strength during the deglaciation (14 ka to 8 ka) and reverses flow direction beneath the transition margin from the craton to the oceanic plate to the present (Figures 10i and 10l). In addition, the TX19 model predicts a horizontal flow away from the load center at 14 ka within the low viscosity zone beneath the North American Cordillera (Figure 11g), which causes southward surface motion within the former ice cover, in contrast to the inward surface motion centered at Hudson Bay for 1D_REF and 3D_T_e. This motion is redirected northward with the Laurentide ice sheet margin progressively retreating northward to Hudson Bay around 8 ka (Figure 11h). During the subsequent free decay, the return flow channels more horizontally toward the ice center within the low viscosity mantle, producing the present-day northward surface motion over North America for TX19 (Figures 5d and 11i). The horizontal flow predicted by the REVEAL model is slightly weaker at present day, with persistent northern flow direction from 14 ka to present, and small-scale alternating weak and stiff viscosity structures may compensate for one another (Figures 9d and 11l). Note the reversal mantle return flow beneath the southern margin of the former ice cover, observed in the 1D_REF model (~40°–50°N; Figure 11c), is diminished in the 3D_T_e model and has not yet developed in either of the two LVV models (Figures 11i and 11l).

Figures 10 and 11 also show the temporal evolution of the deviatoric strain rate. In 1D_REF and 3D_Te, shear deformation is concentrated beneath the former ice load, while the weak asthenosphere in the LVV models produces significantly larger strain rates beneath the oceanic lithosphere. In contrast, the elastic lithosphere shows negligible deviatoric strain rates in both 1D and 3D models. To further analyze the balance between shear and rotations due to flexure, which may be of help when analyzing GIA induced seismicity, for example, we also show the ratio between the amplitude of vorticity and strain rate in the same cross sections (Figures S2, S3 and S5, S6 in Supporting Information S1). This ratio is also defined as kinematical vorticity number $W_K = \frac{\sqrt{\omega_k \omega_k}}{\sqrt{2\dot{\epsilon}_{ik}\,\dot{\epsilon}_{ik}}}$, where ω_k is vorticity and $\dot{\epsilon}_{ik}$ is strain rate tensor (e.g., Ivins, 1989; Truesdell, 1953). The results show that the regions of maximum shear correspond to minimum kinematical vorticity number (e.g., Figure 10j and Figures S1j vs. S2j in Supporting Information S1). Furthermore, rigid-body rotation is concentrated at the edges of the continental lithosphere beneath the former ice margin, with an intensified kinematical vorticity number in the present-day deformation field for both 3D cases.

4. Discussion

4.1. Surface Motion Sensitivity on the Vertical Variations in Viscosity Profile

Both the TX19 and REVEAL LVV models, together with the VM5a-type 1D viscosity structure (1D_REF), predict northward present-day surface motion over the formerly glaciated Laurentide region. The horizontal channeling of mantle return flow through the low-viscosity zone significantly influences the evolution of surface motion following the last deglaciation. To investigate how the surface motion patterns depend on lateral and vertical viscosity variations, we conducted a set of tests.

Although our 3D viscosity models are tuned to match its regional average in North America with the reference model in 1D_REF, the locally depth-averaged variations can still deviate from the 1D structure. To test the sensitivity of surface motion to the vertical deviation of 3D viscosity from the 1D model, we build a set of 1D models that capture different anomaly structures in 3D. Figure 12 shows 1D viscosity structures with a three-layer profile (dotted gray curve) and a refined structure with six-layer profile (dashed red curve) to approximate the local depth-averaged 3D viscosity variations in TX19 in the west Hudson Bay (blue curve). While the 3-layer viscosity represents the large-scale variations between upper and lower mantle in 3D, the 6-layer model captures refined structure such as the stiff continental root, the weak asthenosphere and high-viscosity lower mantle anomaly beneath the Canadian Shield. The present-day horizontal motion is distinct between the two 1D viscosity profiles: the 3-layer model predicts an outward motion around the rebound center, whereas the six-layer model predicts inward horizontal motion (Figures 13a and 13b).

To understand the dominant factor responsible for the opposed horizontal motion, we construct hybrid cases, where the 3-layer model is modified by replacing one layer at a time with the corresponding layer from the 6-layer profile. For example, Figure 13c shows the surface motion for the hybrid case with layer 1 in the 6-layer model (Figure 12) superimposed on to the 3-layer model. Comparing Figures 13c–13h, we find that the inward horizontal motion can only be predicted when layer 2 is superimposed on the 1D model, indicating the increase in mantle viscosity with ~ one order of magnitude within 100–400 km depths controls the surface motion pattern, and the viscosity changes in other layers modulate the strength. We also constructed viscosity model with more layers in the shallow depths and found the inward pattern persists across those cases. In the refined models (six or more layers) with a stiffer shallow upper mantle, the horizontal motions remains inward from ~14 ka to the present, while the three-layer model with a weaker shallow upper mantle predicts a transition from inward to outward around 8 ka, followed by a reduced outward signal at the present day (cf. Figure 5).

Our results indicate that the upper mantle viscosity, particularly in shallow depths beneath the lithosphere, can significantly change the timescale of the horizontal motion relaxation after deglaciation and induce distinct patterns of surface horizontal motion at present day. Together with the mantle flow results, this indicates that the greater sensitivity of the horizontal motion to the shallow structure than the verticals stem from differences in the relaxation pathways of glaciation induced mantle flow. Our results support the finding of Milne et al. (2004) and

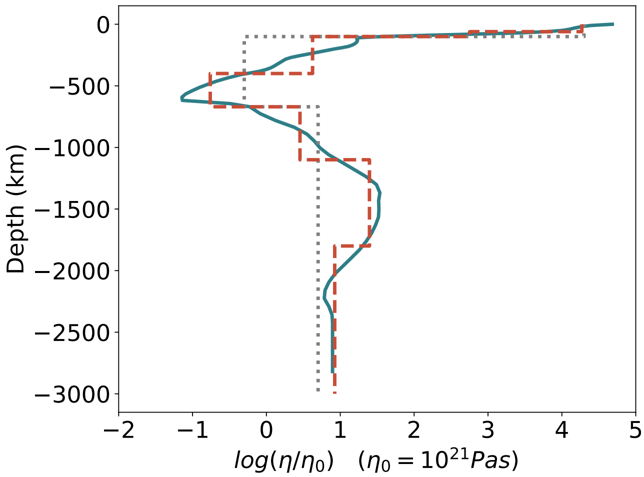

Figure 12. Viscosity profiles for the depth-averaged 3D viscosity model for TX19 (blue) around Hudson Bay, compared with a three-layer 1D proximation (dotted gray) and a six-layer 1D proximation (dashed red).

Wu (2006) that the largest sensitivity lies in the shallow part of the upper mantle, which significantly impacts the direction of the surface horizontal motion. Our results also confirm the significant sensitivity in the lower part of the upper mantle reported by Steffen et al. (2007) and Lau et al. (2018); viscosity anomalies in this depth range significantly affect the amplitude of surface motion (Figures 13a vs 13e), but do not alter the horizontal divergence pattern (i.e., the inward vs. outward flow direction). The 40 km thick sub-lithospheric layer with viscosity of 6.3 × 10^{22} Pas we incorporated beneath the 60 km elastic lithosphere does not significantly affect the predicted horizontal surface motion (Figures 13a vs 13c), which contrasts with the findings in Argus and Peltier (2010) for VM5a. This discrepancy reflects the inherent uncertainties in lithospheric structure in GIA modeling.

4.2. Surface Motion Sensitivity on Lateral Structure

A model with homogenous mantle but laterally variable lithosphere thickness shows divergent motion centered around Hudson Bay (e.g., 3D_T_e in Figure 5a), consistent with the pattern for 1D_REF (Figure 5b) but induces strong convergent motion beyond the LGM ice margin (e.g., regions with thin lithosphere thickness around the Pacific coast and the southern part of U.S.). This substantiates that the sensitivity of GIA-predicted RSL to lithospheric thickness near and beyond the peripheral bulge (e.g., Zhong et al., 2003) also applies to horizontal motion.

To isolate the effect of LVVs for surface motion, we conduct an end member of models with lateral viscosity variations from the surface to the CMB without the high-viscosity lithosphere layer. This model predicts a convergent horizontal motion with an amplitude about five times larger (Figure 14b); without the effect of lithospheric flexure, the mantle continues to flow inward toward the ice center (Figure 15a). This surface motion remains centered around Hudson Bay even when LVVs are considered. When both variable T_e and LVVs are

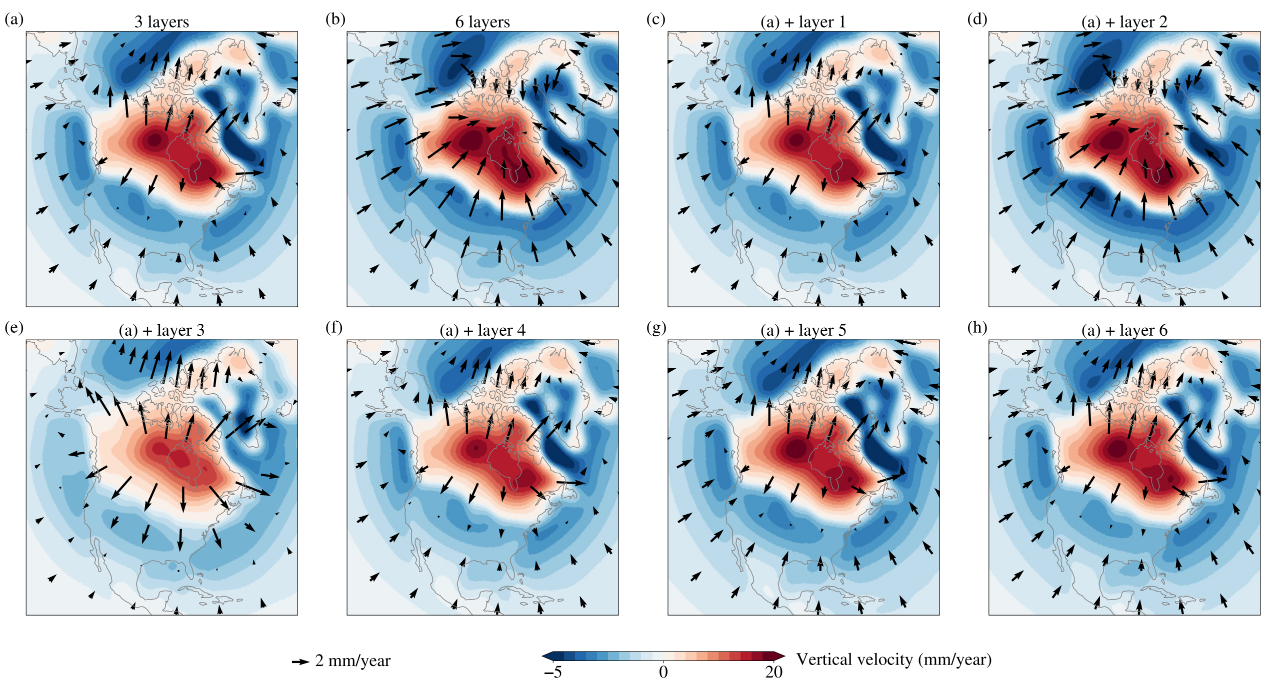

Figure 13. Present-day vertical and horizontal velocity fields for different 1D viscosity structures: (a) three-layer model (dotted gray in Figure 12); (b) six-layer model (dotted-dashed red in Figure 12); (c)–(h) hybrid cases, where the three-layer model is modified by replacing one layer at a time with the corresponding layer from the six-layer profile. For example, (d) shows surface motion for the 1D viscosity structure combining the three-layer model (dotted gray in Figure 12) with the second layer (∼100–400 km depth) from the six-layer profile (dashed red curve in Figure 12).

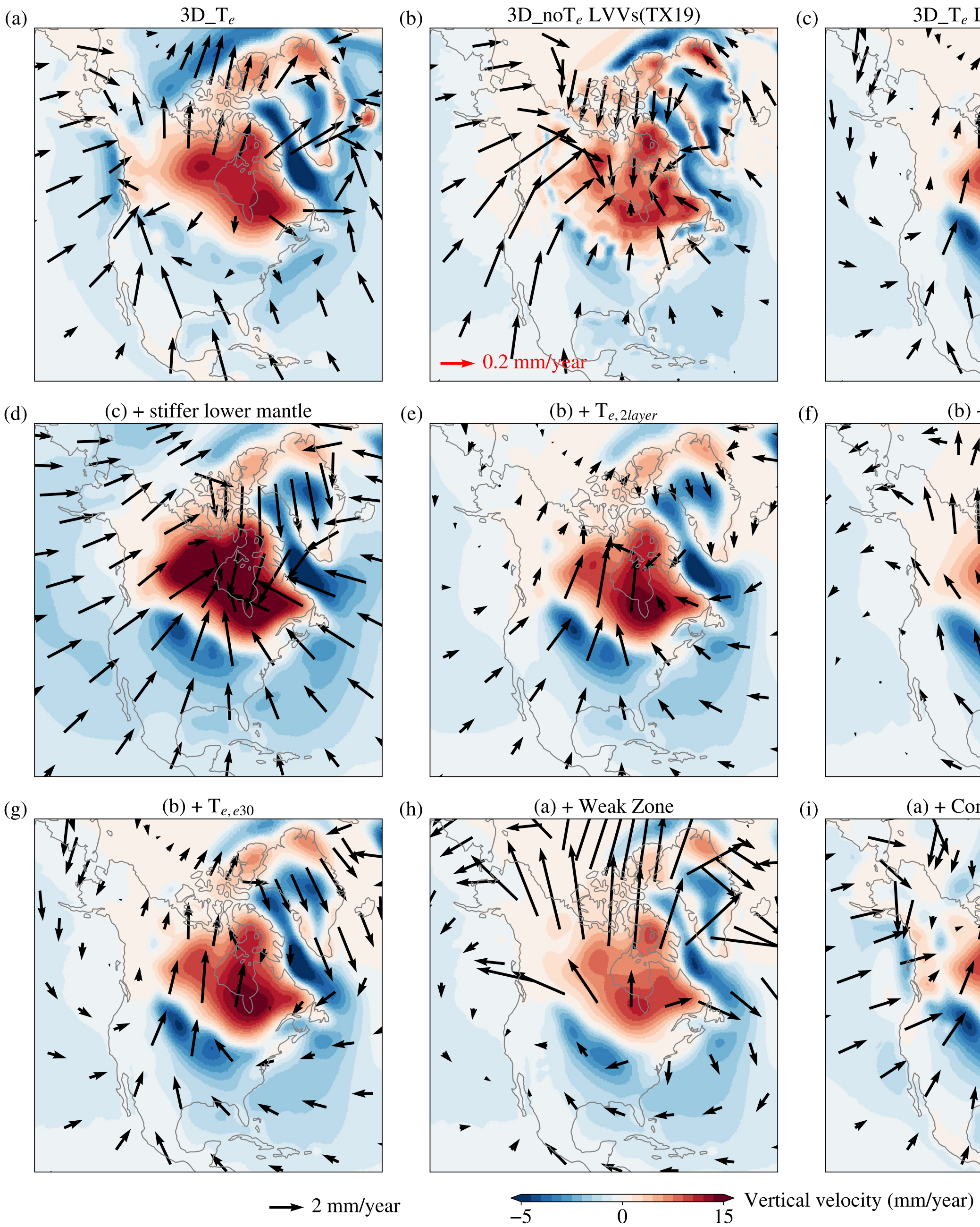

Figure 14. Present-day surface vertical and horizontal velocity fields for different 3D viscosity structures, including (a) variable lithosphere thickness T_e with viscosity as 10^{26} Pa s; (b) lateral viscosity variations (LVVs) but no lithosphere; (c) variable lithosphere thickness T_e and LVVs from TX19; (d) same as (c) but for stiffer lower mantle viscosity with 10^{22} Pa s in 1D reference; (e) LVVs with variable T_e but having a weak sub-lithosphere structure by assigning a viscosity of 10^{22} Pa s below 60 km within the T_e layer; (f) LVVs with variable T_e with a global average as ∼97 km thickness; (g) LVVs with variable T_e with viscosity as 10^{30} Pa s; (h) variable T_e and oceanic weak zone only; (i) variable T_e and stiff continental root only. Note the scale in (b) is 10 times larger than these in other panels.

included (Figure 14c), the Hudson Bay centered motion observed in the model with only T_e variable or LVV considered are overprinted by a northward motion over former glaciated region.

We also tested the impact of lower mantle viscosity on the surface motion by replacing the reference lower mantle viscosity in 3D_T$_e$_LVVs(TX19) with a higher viscosity of 10^{22} Pa s. With stiffer lower mantle the surface motion shows a convergent pattern centered around Hudson Bay (Figure 14d). The stiffer lower mantle with a longer relaxation time slows down the forming of the shallow reversal upper mantle flow, causing the convergent

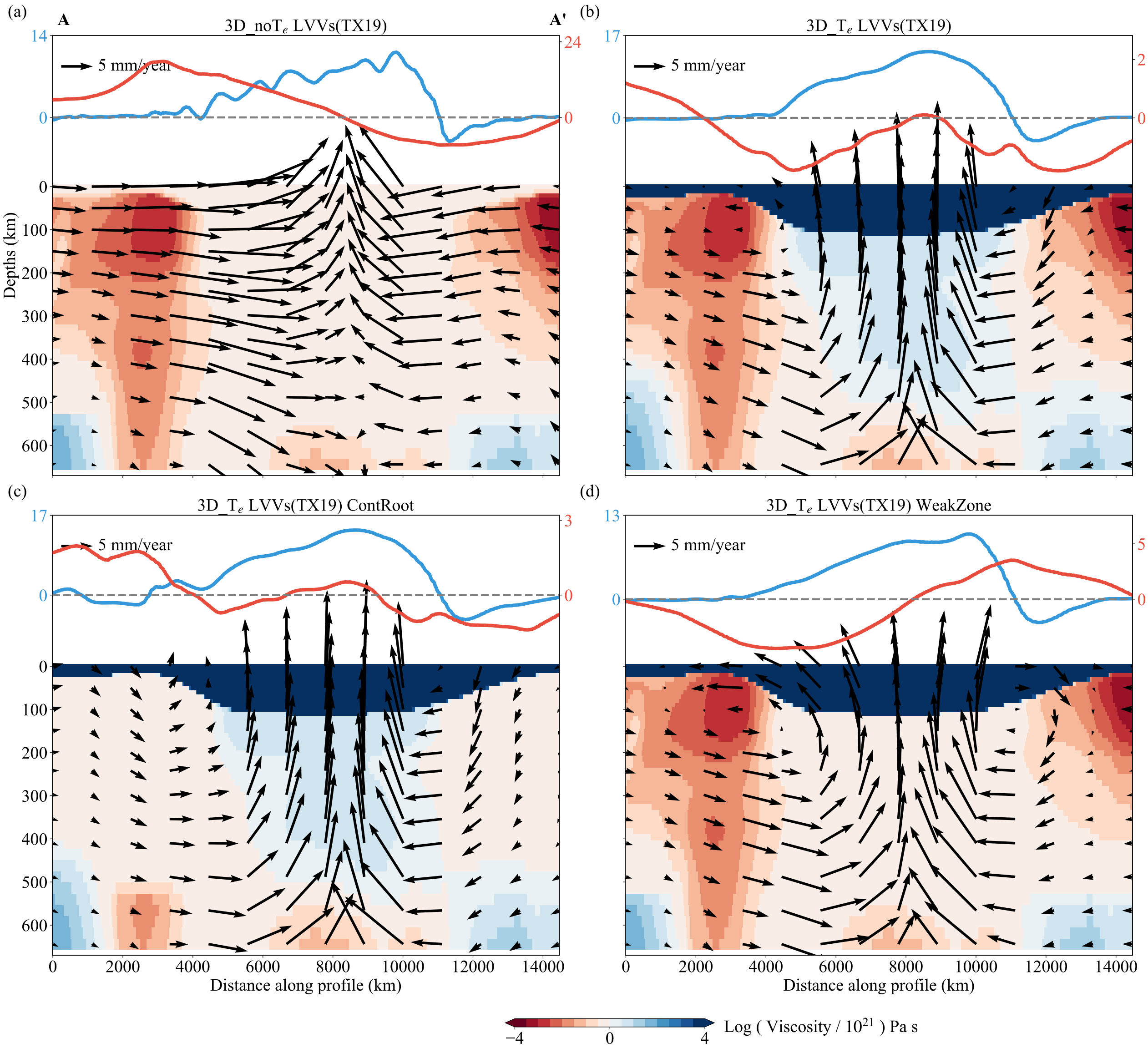

Figure 15. Cross sections for present-day GIA-induced mantle flow velocities along profile A-A′ in Figure 1 for different 3D viscosity structures, including (a) lateral viscosity variations (LVVs) but no lithosphere; (b) variable lithosphere thickness T_e and LVVs from TX19; (c) variable T_e and oceanic weak zone only; and (d) variable T_e and stiff continental root only. Other plot features are the same as in Figure 8.

surface motion at present day. The Hudson Bay centered motion in Figure 14d also suggests the stiff lower mantle with averaged viscosity of 10^{22} Pa s can mask the center-shifted horizontal motion associated with the lithosphere-upper mantle interplay in Figure 14c. Wu (2005) and Wang and Wu (2006) reported that lateral heterogeneity can weaken or completely overprint the divergent mantle flow predicted by laterally homogeneous models in Laurentia, and indicated this effect arises from contributions of the deep lower mantle. Our results emphasize that changes in the spatial pattern (e.g., deviation of horizontal motion from the Hudson Bay center) arise from the interaction between the elastic lithosphere flexure and the heterogeneous viscous drag in the shallow mantle, while the lower mantle can further modulate the timescale of the coupled relaxation, thereby altering the snapshot of the surface horizontal pattern at present-day.

The strength of the lithosphere flexure in GIA model depends, of course, on both the viscosity structure and the mechanical thickness of the lithosphere. Argus and Peltier (2010) and Peltier et al. (2015) suggest that by introducing a sub-lithosphere layer with high viscosity of 10^{22} Pa s in VM5a, their model greatly improves the fit of the horizontal observations. Our 1D models in Figures 5a and 5b confirm their conclusion, producing

10.1029/2025JB033462

diminished outward motion over Canada. This is also evident in the time series shown in Figure 6b, where VM5a predicts a smaller extensional deformation than both the 1D_REF and 3D_REF models, which share a comparable regional lithospheric thickness of ~100 km T_e over the Hudson Bay. However, timing is important, and the evolution of the spatial pattern (Figure 7) and the regionally averaged horizontal divergence (Figure 6b) suggest that the weaker sub-lithosphere in the VM5a model leads to a slower formation of the reversal mantle return flow, resulting in a 2–3 ky delay in the horizontal motion reversal relative to the one-layer lithosphere model in 1D_REF. The delayed phase is further reflected in the similarity between the present-day horizontal motion in the VM5a case (Figure 7, first column, 0 ka) and the motion at 4 ka in the one-layer lithosphere model 1D_REF (Figure 7, second column, 4 ka).

For 3D_T_e_LVVs(TX19), we further examined the effect of a weak sub-lithosphere by assigning a viscosity of 10^{22} Pa s below 60 km within the T_e layer (Figure 14e). The resulting surface motion pattern and amplitude closely resemble those of the model without this layer, indicating that lithospheric strength in the 3D configuration is primarily governed by lateral variations in T_e, with a lesser dependence on viscosity. This conclusion is further supported by two cases. First, a model with a larger global average T_e of 97 km, which gives the thickest lithosphere under the ice center as ~ 230 km, predicts noticeable changes in the surface motion pattern, such as the northwestern motion west of North America (Figure 14f). A thicker lithosphere enhances the return flow underneath the West Coast and induces a return flow started underneath the East Coast. Second, a model with the same T_e but an even higher viscosity of 10^{30} Pa s shows the horizontal motion mostly identical to that of the 3D_T_e_LVVs (TX19) with 10^{26} Pas, indicating that in both cases the lithosphere behaves elastically, consistent with Maxwell timescales on the order of tens of millions of years and above (Figure 14g).

Lateral viscosity variations in the upper mantle beneath North America are dominated by cratonic roots and sub-oceanic asthenosphere on large scales. We isolate the impact of these structures by constructing two cases with only the weak oceanic mantle included and only the continental root included. The weak asthenosphere enhances mantle return flow and channels it more horizontally, producing divergent surface motion with larger amplitude (Figures 14h and 15d). In contrast, the stiff craton prolongs relaxation beneath the ice load, suppresses the strength of the turning flow, directing the flow more vertically at shallow depths (Figures 14i and 15c; Figure S7 in Supporting Information S1).

Our results indicate that while the vertical motion around the former ice center is in-phase with surface loading, horizontal motions exhibit complex evolutionary paths with an out-of-phase relaxation with surface loading and motion reversal over the former ice cover. Hermans et al. (2018) reported similar reversal of horizontal velocities based on a homogenous GIA model, and indicate present-day horizontal velocities point outward for a uniform mantle viscosity below 10^{20} Pa s and inward above 10^{22} Pa s. Our results substantiate their conclusions. However, lateral heterogeneity in both lithosphere and mantle, decreasing lithosphere thickness from the ice center to the ice margin (e.g., from Hudson Bay to the West Coast), together with the craton to sub-oceanic asthenosphere transition away from the load center, can significantly change the circular pattern of the mantle return flow and hence induce distinct surface horizontal motions. As discussed by Brandes et al. (2025), for example, forebulge formation involves elastic and viscous bending deformation of the lithosphere, whereas mantle viscosity affects forebulge migration and decay. Within this context, our findings highlight how the timing, strength and spatial pattern of mantle circulation can impact the geometry and temporal evolution of the forebulge.

4.3. The Reversal Timing of the Surface Horizontal Velocity

During ice melting, the viscous drag along the lithosphere-asthenosphere boundary (LAB) interacts with lithospheric flexure, driving the lithosphere to uplift and migrate inward toward the ice center. Following largely complete deglaciation, the surface load is significantly reduced, and the mantle subsequently relaxes through viscous deformation. As the viscous drag on the LAB diminishes, elastic flexure of the lithospheric bulge dominates, driving outward motion in its shallow portion. To see how visco-elastic relaxation times can represent this process, we approximate typical relaxation times, τ, using a simple, Cartesian 2D model with an elastic plate overlying a viscous half space relaxing topography with wave number $k = \frac{2\pi}{\lambda}$, λ is the load wavelength (Equation 5; Turcotte & Schubert, 2002):

$$\tau(k) = \frac{2\eta k}{Dk^4 + \rho g} \tag{5}$$

Table 2
Summary of Parameters

Parameter	Value
Shear modulus μ	9.78×10^{10}
Poisson's ratio ν	0.25
Density ρ	3,583
Gravitational acceleration g	9.81
Wavelength λ	1,000 km

Here, η is the viscosity, D is the flexural rigidity ($D = \frac{2}{9}\mu h^3$ with Poisson's ratio $\nu = 0.25$, where μ is the shear modulus, h is the elastic plate thickness), ρ is the density of the viscous fluid, and g is gravitational acceleration. We use the regional average T_e over North America as the elastic plate thickness h, and the volumetric average from the lithosphere base to 670 km depth over North America as η. Other parameters are listed in Table 2, in which the shear modulus and density are the volumetric averages from 100 to 670 km in PREM. It should be noted that Equation 5 assumes a load of constant wavelength, analogous to a step-function loading history, whereas the realistic ice load undergoes progressive shrinkage with a decreasing characteristic wavelength over time. As the ice retreats and λ shrinks from 4,000 km at LGM to mostly load-free at ∼6 ka, we estimate τ at a characteristic wavelength of 1,000 km representative of the Hudson Bay load at the late deglaciation period.

Figure 16 presents the relationship between the surface horizontal vector reversal time and the relaxation time for eight 1D models and eight 3D models considered before. We also tested $\lambda = 4{,}000$ km representative of the Laurentide Ice Sheet during the early deglaciation (Figure S8 in Supporting Information S1).

Our results show a roughly linear relationship between this estimate of the visco-elastic relaxation time and the time of reversal of horizontal motions. Among models with the same lithospheric structure, 3D LVVs models with larger regional-averaged viscosity over Hudson Bay have relaxation times of 5–6 ky, with reversal times near the present day (e.g., 3D_Te_LVVs(TX19) and 3D_Te_LVVs(REVEAL)), while those with smaller regional-averaged viscosity have relaxation times of 3–4 ky and earlier reversal times (e.g., 3D_Te and 3D_Te_LVVs (TX19)WeakZone). The reversal time is also sensitive to lithospheric thickness (e.g., VM5a, 1D_REF, 3D_Te, and the two groups of 3-layer 1D models), where a thicker T_e corresponds to an earlier reversal time. At the characteristic wavelength of 1,000 km, the relaxation time reflects contributions from both the elastic plate and the viscous fluid. The model with the weakest mantle viscosity and thickest T_e (e.g., the orange circle, 1D(146/0.2/1)) has the smallest relaxation time (<1 ky) and the earliest reversal time of ∼10 ky BP. The variable T_e model has a smaller flexural rigidity than 1D_REF, resulting in a ∼1 ky longer relaxation time and a 200–300 years delayed reversal time (e.g., red triangle for 3D_Te vs. green circle for 1D_REF). With LVVs included, the continental root increases the depth-averaged viscosity from 0.48×10^{21} Pas in 3D_Te to 0.85×10^{21} Pas in 3D_Te_LVVs, slowing the relaxation to $\tau = 5$–6 ky and delaying the reversal time to roughly the present day, as discussed above.

At long wavelengths of 4,000 km relevant to Laurentide ice sheet at earlier deglaciation period, the linear relationship between the relaxation time and the reversal time still holds roughly (Figure S8 in Supporting Information S1). However, at longer wavelengths gravity dominates the restoring force ($\rho g \gg Dk^4$, Equation 2), and the relaxation time becomes insensitive to T_e. Therefore, models with similar mantle viscosity structure but different T_e show nearly identical relaxation times, and the linear relationship in Figure S8 in Supporting Information S1 primarily reflects the control of mantle viscosity on the reversal time.

4.4. Implications for Present-Day Crustal Deformation

The influence of lateral heterogeneities governing postglacial upper mantle circulation and surface motions can provide insights into the processes contribution to geodetically constrained surface deformation. We suggest that GNSS horizontals (Figure 1) show contributions from regional, GIA induced mantle return flow. While the different LVV models predict comparable, broad scale dilatation at present-day, they can differ significantly at the local scale. One example is the region southwest of Hudson Bay, where TX19 predicts extensional dilatation while REVEAL predicts negative (compressional) dilatation, reflecting the influence of the localized low

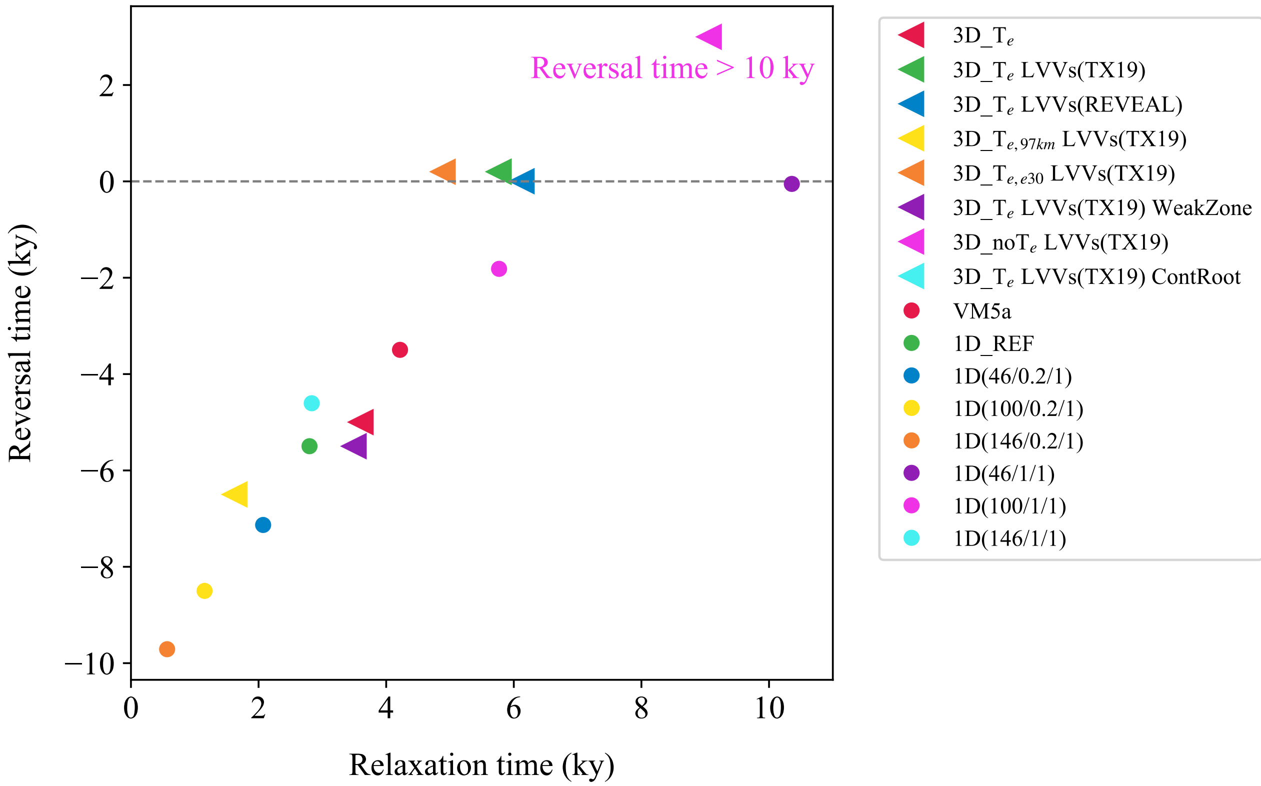

Figure 16. Relaxation time τ (Equation 2) versus surface horizontal velocity reversal time for eight 1D models (circles) and eight 3D models (triangles), computed at a characteristic wavelength of $\lambda = 1{,}000$ km representative of the residual Hudson Bay ice load during late deglaciation. The relaxation time is estimated using the regional average elastic lithosphere thickness T_e and the depth-averaged mantle viscosity from the base of the lithosphere to 670 km depth over North America, together with other parameters in Table 2. The dashed line indicates the present day. The model with only the continental root, having a depth-averaged viscosity of 2.12×10^{21} Pas, has a relaxation time of ∼15 ky, which falls outside the *x*-axis range and is therefore not shown.

viscosity anomaly at 400–600 km depth inferred from REVEAL which is not derived from the longer wavelength TX19 model. The persistent northward motion induced by the low viscosity zone beneath the western North America Cordillera appears not supported by observations. This may imply that we underestimate mantle viscosity for this region in our model, perhaps because the slow seismic velocity anomalies in the asthenosphere are less indicative of temperature variations, and more greatly impacted by composition or partial melt (e.g., Liu & King, 2022). Moreover, while the VM5a 1D viscosity profile paired with the ICE-6G_C ice model are constructed to fit the key GIA data sets using a 1D symmetrical Earth, either one, or both, may have to be revised for 3D GIA model construction, causing potential biases in the interpretation of observations.

The large lateral contrast between oceanic and continental lithospheric thickness along the West Coast of North America generates strong surface compressional deformation at present-day that is captured by the 3D lithospheric thickness model but absent in 1D. The horizontal mantle return flow driven by the weak oceanic upper mantle suppresses the formation of strong compressional surface deformation in the 3D model. This coupling between lithospheric flexure and the shallow part of the upper mantle highlights the necessity of incorporating lateral variations in both layers simultaneously in GIA modeling to accurately capture the physical processes and interpret surface deformation. This is especially important for the interpretation of GNSS data along the West Coast of North America where the interplay between these two layers produces distinct surface patterns that neither 1D models nor 3D models incorporating lateral variations in only one of these layers can adequately reproduce.

The laterally varying mantle structure beneath the LGM ice cover significantly modifies the evolutionary pathway of surface dilatation following deglaciation. The strong continental root affects the rate of surface dilatation change during the relaxation period, delaying the transition from compressional to extensional. As a result, large residual compressional deformation and elevated horizontal velocities persist around Hudson Bay at present-day.

This suggests that lateral viscosity variations beneath former ice sheets may have the capacity to sustain a relatively thicker ice sheet with a faster and/or sooner melting during deglaciation, with implications for reconstructions of ice sheet history.

The thin oceanic lithosphere overlying the weak asthenosphere near the western margin of the Cordilleran Ice Sheet produces strong shear flow in the shallow upper mantle during the rapid ice melting at ∼14 ka. This flow induces significant bedrock uplift near the ice sheet margin, and pronounced bedrock subsidence beyond (e.g., Figures 10g and 10j), which may influence ice sheet dynamics (Gomez et al., 2018; Huang et al., 2019; Van Calcar et al., 2023). Furthermore, the large uplift and horizontal inward motion near the ice margin, indicative of tilting, modifies the bedrock slope which may further impact ice dynamics. This effect may be significant for marine-based ice sheet evolution elsewhere, for example, for the West Antarctic Ice Sheet, which shares a similar setting.

In order to better constrain the details of these complex relaxation processes for a 3D lithosphere-asthenosphere system, the formation of crystallographic preferred orientation fabrics in olivine in the asthenosphere as imaged by seismic anisotropy may provide another constraint for postglacial mantle return flow. This indicates a potential avenue for joint geodetic and seismological study of the shear flow associated with GIA. The delayed mantle return flow and the potentially lagged timing of the horizontal velocity reversal identified in 3D LVV models may also have important implications for GIA-induced seismicity (cf. Hightower & Gurnis, 2025), as the sustained deviatoric stresses associated with ongoing postglacial adjustment could continue to modulate intraplate fault reactivation well beyond the period of active deglaciation.

5. Conclusion

We investigate how lateral heterogeneities in the lithosphere and mantle can influence postglacial mantle return flow and associated surface deformation. While vertical crustal motions are in phase with ice loading, horizontal divergence can be out of phase with both the ice loading and verticals. At the onset of the last deglaciation, the vertical velocity near the former ice center transitions from subsidence to sustained uplift. In contrast, horizontal motions show a delayed transition from positive to negative horizontal divergence following the onset of ice retreat at the LGM (∼26 ka) and subsequently reverse again from negative to positive as deglaciation proceeds. The reversal time scales with a visco-elastic relaxation time, which depends on both the lithospheric flexural rigidity and the mantle viscosity.

The formation and evolution of the associated circulation pattern provides new insights into peripheral GIA bulge dynamics. A thin oceanic lithosphere promotes stronger far-field return flow and confines mantle circulation to the transition region between craton and adjacent oceanic plates underneath North America, for example, The weak oceanic asthenosphere off to the west enables shear while the continental root underneath the central U.S. promotes vertical upwelling at its edges, together producing a circulation pattern which may be detected by joint seismic anisotropy and geodetic studies. A stiff continental root also significantly delays the formation of this circulation underneath Laurentia, with the reversal of surface horizontal motion occurring quite recently.

These complex dynamics highlight the necessity of incorporating lateral variations in lithosphere structure and upper mantle viscosity simultaneously in GIA modeling to accurately capture the underlying physical processes and reproduce geodetically observed surface deformation patterns. Our results also imply that small-scale viscosity anomalies in the middle to deep upper mantle can significantly influence far-field surface horizontal velocity pattern. Such peripheral bulge dynamics and the tilting of the continental lithosphere warrant further investigation through coupled ice sheet-GIA modeling and GIA-induced seismicity.

Conflict of Interest

The authors declare no conflicts of interest relevant to this study.

Availability Statement

The ICE-6G_C ice history model is described in Peltier et al. (2015). The analytic GIA software is available in Kang et al. (2025). The finite element package CitcomSVE3 is available in Yuan et al. (2025). The model outputs generated in this study using 3D Earth structures (3D_Te, 3D_Te_LVVs(TX19) and 3D_Te_LVVs(REVEAL)), including vertical and horizontal land motion rates from 122 ka to present-day and predictions 10 ky into the future, are available through Zenodo (https://doi.org/10.5281/zenodo.17681998). Figures were made with Matplotlib version 3.2.1 (Caswell et al., 2020) and Cartopy 0.24.1 (Cartopy Contributors, 2024), available under the Matplotlib license at http://matplotlib.org/ and https://github.com/SciTools/cartopy.

Acknowledgments
We thank Shijie Zhong and Tao Yuan for making the finite element package CitcomSVE3 available and are grateful for the constructive reviews provided by Erik Ivins and an anonymous reviewer which helped to improve a previous version of this manuscript. We also thank Steve Nerem and Ashley Bellas-Manley for valuable discussions. KK and TWB were partially supported by NSF EAR-1921474 and EAR-2045292.

References

Argus, D. F., & Peltier, W. R. (2010). Constraining models of postglacial rebound using space geodesy: A detailed assessment of model ICE-5G (VM2) and its relatives. *Geophysical Journal International*, *181*(2), 697–723. https://doi.org/10.1111/j.1365-246x.2010.04562.x

Argus, D. F., Peltier, W. R., Blewitt, G., & Kreemer, C. (2021). The viscosity of the top third of the lower mantle estimated using GPS, GRACE, and relative sea level measurements of glacial isostatic adjustment. *Journal of Geophysical Research: Solid Earth*, *126*(5), e2020JB021537. https://doi.org/10.1029/2020jb021537

Audet, P., & Bürgmann, R. (2011). Dominant role of tectonic inheritance in supercontinent cycles. *Nature Geoscience*, *4*(3), 184–187. https://doi.org/10.1038/ngeo1080

Bagge, M., Klemann, V., Steinberger, B., Latinović, M., & Thomas, M. (2021). Glacial-isostatic adjustment models using geodynamically constrained 3D Earth structures. *Geochemistry, Geophysics, Geosystems*, *22*(11), e2021GC009853. https://doi.org/10.1029/2021gc009853

Barletta, V. R., Bevis, M., Smith, B. E., Wilson, T., Brown, A., Bordoni, A., et al. (2018). Observed rapid bedrock uplift in Amundsen Sea Embayment promotes ice-sheet stability. *Science*, *360*(6395), 1335–1339. https://doi.org/10.1126/science.aao1447

Bechtel, T. D., Forsyth, D. W., Sharpton, V. L., & Grieve, R. A. (1990). Variations in effective elastic thickness of the North American lithosphere. *Nature*, *343*(6259), 636–638. https://doi.org/10.1038/343636a0

Becker, T. W. (2006). On the effect of temperature and strain-rate dependent viscosity on global mantle flow, net rotation, and plate-driving forces. *Geophysical Journal International*, *167*(2), 943–957. https://doi.org/10.1111/j.1365-246x.2006.03172.x

Book, C., Hoffman, M. J., Kachuck, S. B., Hillebrand, T. R., Price, S. F., Perego, M., & Bassis, J. N. (2022). Stabilizing effect of bedrock uplift on retreat of Thwaites Glacier, Antarctica, at centennial timescales. *Earth and Planetary Science Letters*, *597*, 117798. https://doi.org/10.1016/j.epsl.2022.117798

Brandes, C., Steffen, H., Steffen, R., Li, T., & Wu, P. (2025). Effects of the last Quaternary glacial forebulge on vertical land movement, sea-level change, and lithospheric stresses. *Reviews of Geophysics*, *63*(3), e2024RG000852. https://doi.org/10.1029/2024rg000852

Cartopy Contributors. (2024). Cartopy: A Python package designed to make drawing maps for data analysis and visualization easy [Software]. *Zenodo*. https://doi.org/10.5281/zenodo.13905945

Caswell, T. A., Droettboom, M., Lee, A., de Andrade, E. S., Hunter, J., Firing, E., et al. (2020). matplotlib/matplotlib v3.2.1 [Software]. *Zenodo*. https://doi.org/10.5281/zenodo.3714460

Chopelas, A., & Boehler, R. (1992). Thermal expansivity in the lower mantle. *Geophysical Research Letters*, *19*(19), 1983–1986. https://doi.org/10.1029/92gl02144

Crawford, O., Al-Attar, D., Tromp, J., Mitrovica, J. X., Austermann, J., & Lau, H. C. (2018). Quantifying the sensitivity of post-glacial sea level change to laterally varying viscosity. *Geophysical Journal International*, *214*(2), 1324–1363. https://doi.org/10.1093/gji/ggy184

Dziewonski, A. M., & Anderson, D. L. (1981). Preliminary reference Earth model. *Physics of the Earth and Planetary Interiors*, *25*(4), 297–356. https://doi.org/10.1016/0031-9201(81)90046-7

Faccenna, C., Becker, T. W., Miller, M. S., Serpelloni, E., & Willett, S. D. (2014). Isostasy, dynamic topography, and the elevation of the Apennines of Italy. *Earth and Planetary Science Letters*, *407*, 163–174. https://doi.org/10.1016/j.epsl.2014.09.027

Farrell, W., & Clark, J. A. (1976). On postglacial sea level. *Geophysical Journal of the Royal Astronomical Society*, *46*(3), 647–667. https://doi.org/10.1111/j.1365-246x.1976.tb01252.x

Forte, A. M., & Woodward, R. L. (1997). Seismic-geodynamic constraints on three-dimensional structure, vertical flow, and heat transfer in the mantle. *Journal of Geophysical Research*, *102*(B8), 17981–17994. https://doi.org/10.1029/97jb01276

Gasperini, P., Sabadini, R., & Yuen, D. A. (1991). Deep continental roots: The effects of lateral variations of viscosity on post-glacial rebound. In *Glacial isostasy, sea-level and mantle rheology* (pp. 21–32). Springer Netherlands.

Gasperini, P., Yuen, D. A., & Sabadini, R. (1990). Effects of lateral viscosity variations on postglacial rebound: Implications for recent sea-level trends. *Geophysical Research Letters*, *17*(1), 5–8. https://doi.org/10.1029/gl017i001p00005

Gomez, N., Latychev, K., & Pollard, D. (2018). A coupled ice sheet–sea level model incorporating 3D Earth structure: Variations in Antarctica during the last deglacial retreat. *Journal of Climate*, *31*(10), 4041–4054. https://doi.org/10.1175/jcli-d-17-0352.1

Gomez, N., Mitrovica, J. X., Huybers, P., & Clark, P. U. (2010). Sea level as a stabilizing factor for marine-ice-sheet grounding lines. *Nature Geoscience*, *3*(12), 850–853. https://doi.org/10.1038/ngeo1012

Hermans, T. H. J., van der Wal, W., & Broerse, T. (2018). Reversal of the direction of horizontal velocities induced by GIA as a function of mantle viscosity. *Geophysical Research Letters*, *45*(18), 9597–9604. https://doi.org/10.1029/2018gl078533

Hightower, E., & Gurnis, M. (2025). Influence of glacial isostatic adjustment on intraplate stress and seismicity in eastern North America in the presence of pre-existing weak zones. *Geochemistry, Geophysics, Geosystems*, *26*(10), e2025GC012290. https://doi.org/10.1029/2025gc012290

Hua, J., Schulte-Pelkum, V., Becker, T. W., He, B., & Zhu, H. (2025). Waveform effects on shear wave splitting near fault zones. *Journal of Geophysical Research: Solid Earth*, *130*(8), e2025JB031656. https://doi.org/10.1029/2025jb031656

Huang, P., Wu, P., & Steffen, H. (2019). In search of an ice history that is consistent with composite rheology in glacial isostatic adjustment modelling. *Earth and Planetary Science Letters*, *517*, 26–37. https://doi.org/10.1016/j.epsl.2019.04.011

Husson, L., Bodin, T., Spada, G., Choblet, G., & Kreemer, C. (2018). Bayesian surface reconstruction of geodetic uplift rates: Mapping the global fingerprint of glacial isostatic adjustment. *Journal of Geodynamics*, *122*, 25–40. https://doi.org/10.1016/j.jog.2018.10.002

Ivins, E. R. (1989). New aspects of rotational dynamics within the North American-Pacific Ductile Shear Zone. *Deep Structure and Past Kinematics of Accreted Terranes*, *50*, 179–201.

James, T. S., Gowan, E. J., Wada, I., & Wang, K. (2009). Viscosity of the asthenosphere from glacial isostatic adjustment and subduction dynamics at the northern Cascadia subduction zone, British Columbia, Canada. *Journal of Geophysical Research*, *114*(B4). https://doi.org/10.1029/2008JB006077

James, T. S., & Lambert, A. (1993). A comparison of VLBI data with the ICE-3G glacial rebound model. *Geophysical Research Letters*, *20*(9), 871–874. https://doi.org/10.1029/93gl00865

James, T. S., & Morgan, W. J. (1990). Horizontal motions due to post-glacial rebound. *Geophysical Research Letters*, *17*(7), 957–960. https://doi.org/10.1029/gl017i007p00957

Johnston, P., Lambeck, K., & Wolf, D. (1997). Material versus isobaric internal boundaries in the Earth and their influence on postglacial rebound. *Geophysical Journal International*, *129*(2), 252–268. https://doi.org/10.1111/j.1365-246x.1997.tb01579.x

Kang, K., Yuan, T., & Zhong, S. (2025). Constraints of relative sea level change on the mantle viscosity and the Late Pleistocene deglaciation history [Software]. *Journal of Geophysical Research: Solid Earth*, *130*(3), e2024JB030216. https://doi.org/10.1029/2024JB030216

Kang, K., Zhong, S., Geruo, A., & Mao, W. (2022). The effects of non-Newtonian rheology in the upper mantle on relative sea level change and geodetic observables induced by glacial isostatic adjustment process. *Geophysical Journal International*, *228*(3), 1887–1906. https://doi.org/10.1093/gji/ggab428

Kaufmann, G., & Wu, P. (1998). Lateral asthenospheric viscosity variations and postglacial rebound: A case study for the Barents Sea. *Geophysical Research Letters*, *25*(11), 1963–1966. https://doi.org/10.1029/98gl51505

Kaufmann, G., Wu, P., & Ivins, E. R. (2005). Lateral viscosity variations beneath Antarctica and their implications on regional rebound motions and seismotectonics. *Journal of Geodynamics*, *39*(2), 165–181. https://doi.org/10.1016/j.jog.2004.08.009

Kaufmann, G., Wu, P., & Li, G. (2000). Glacial isostatic adjustment in Fennoscandia for a laterally heterogeneous Earth. *Geophysical Journal International*, *143*(1), 262–273. https://doi.org/10.1046/j.1365-246x.2000.00247.x

Kierulf, H. P., Steffen, H., Simpson, M. J. R., Lidberg, M., Wu, P., & Wang, H. (2014). A GPS velocity field for Fennoscandia and a consistent comparison to glacial isostatic adjustment models. *Journal of Geophysical Research: Solid Earth*, *119*(8), 6613–6629. https://doi.org/10.1002/2013jb010889

Kreemer, C., Hammond, W. C., & Blewitt, G. (2018). A robust estimation of the 3-D intraplate deformation of the North American plate from GPS. *Journal of Geophysical Research: Solid Earth*, *123*(5), 4388–4412. https://doi.org/10.1029/2017jb015257

Lambeck, K., Rouby, H., Purcell, A., Sun, Y., & Sambridge, M. (2014). Sea level and global ice volumes from the Last Glacial Maximum to the Holocene. *Proceedings of the National Academy of Sciences*, *111*(43), 15296–15303. https://doi.org/10.1073/pnas.1411762111

Latychev, K., Mitrovica, J. X., Tromp, J., Tamisiea, M. E., Komatitsch, D., & Christara, C. C. (2005). Glacial isostatic adjustment on 3D Earth models: A finite-volume formulation. *Geophysical Journal International*, *161*(2), 421–444. https://doi.org/10.1111/j.1365-246x.2005.02536.x

Lau, H. C., Mitrovica, J. X., Austermann, J., Crawford, O., Al-Attar, D., & Latychev, K. (2016). Inferences of mantle viscosity based on ice age data sets: Radial structure. *Journal of Geophysical Research: Solid Earth*, *121*(10), 6991–7012. https://doi.org/10.1002/2016jb013043

Lau, H. C. P., Austermann, J., Mitrovica, J. X., Crawford, O., Al-Attar, D., & Latychev, K. (2018). Inferences of mantle viscosity based on ice age data sets: The bias in radial viscosity profiles due to the neglect of laterally heterogeneous viscosity structure. *Journal of Geophysical Research: Solid Earth*, *123*(9), 7237–7252. https://doi.org/10.1029/2018jb015740

Lau, N., Borsa, A. A., & Becker, T. W. (2020). Present-day crustal vertical velocity field for the contiguous United States. *Journal of Geophysical Research: Solid Earth*, *125*(10), e2020JB020066. https://doi.org/10.1029/2020jb020066

Li, T., Khan, N. S., Baranskaya, A. V., Shaw, T. A., Peltier, W. R., Stuhne, G. R., et al. (2022). Influence of 3D Earth structure on glacial isostatic adjustment in the Russian Arctic. *Journal of Geophysical Research: Solid Earth*, *127*(3), e2021JB023631. https://doi.org/10.1029/2021jb023631

Li, T., Wu, P., Steffen, H., & Wang, H. (2018). In search of laterally heterogeneous viscosity models of glacial isostatic adjustment with the ICE-6G_C global ice history model. *Geophysical Journal International*, *214*(2), 1191–1205. https://doi.org/10.1093/gji/ggy181

Li, T., Wu, P., Wang, H., Steffen, H., Khan, N. S., Engelhart, S. E., et al. (2020). Uncertainties of glacial isostatic adjustment model predictions in North America associated with 3D structure. *Geophysical Research Letters*, *47*(10), e2020GL087944. https://doi.org/10.1029/2020gl087944

Liu, S., & King, S. D. (2022). Dynamics of the North American plate: Large-scale driving mechanism from far-field slabs and the interpretation of shallow negative seismic anomalies. *Geochemistry, Geophysics, Geosystems*, *23*(3), e2021GC009808. https://doi.org/10.1029/2021gc009808

Lu, C., Grand, S. P., Lai, H., & Garnero, E. J. (2019). TX2019slab: A new P and S tomography model incorporating subducting slabs. *Journal of Geophysical Research: Solid Earth*, *124*(11), 11549–11567. https://doi.org/10.1029/2019jb017448

Milne, G. A., Davis, J. L., Mitrovica, J. X., Scherneck, H. G., Johansson, J. M., Vermeer, M., & Koivula, H. (2001). Space-geodetic constraints on glacial isostatic adjustment in Fennoscandia. *Science*, *291*(5512), 2381–2385. https://doi.org/10.1126/science.1057022

Milne, G. A., Mitrovica, J. X., Scherneck, H. G., Davis, J. L., Johansson, J. M., Koivula, H., & Vermeer, M. (2004). Continuous GPS measurements of postglacial adjustment in Fennoscandia: 2. Modeling results. *Journal of Geophysical Research*, *109*(B2). https://doi.org/10.1029/2003jb002619

Mitrovica, J., Davis, J., & Shapiro, I. (1994). A spectral formalism for computing three-dimensional deformations due to surface loads: 2. Present-day glacial isostatic adjustment. *Journal of Geophysical Research*, *99*(B4), 7075–7101. https://doi.org/10.1029/93jb03401

Mitrovica, J. X., Wahr, J., Matsuyama, I., & Paulson, A. (2005). The rotational stability of an ice-age Earth. *Geophysical Journal International*, *161*(2), 491–506. https://doi.org/10.1111/j.1365-246x.2005.02609.x

Nield, G. A., Barletta, V. R., Bordoni, A., King, M. A., Whitehouse, P. L., Clarke, P. J., et al. (2014). Rapid bedrock uplift in the Antarctic Peninsula explained by viscoelastic response to recent ice unloading. *Earth and Planetary Science Letters*, *397*, 32–41. https://doi.org/10.1016/j.epsl.2014.04.019

Osei Tutu, A., Sobolev, S. V., Steinberger, B., Popov, A. A., & Rogozhina, I. (2018). Evaluating the influence of plate boundary friction and mantle viscosity on plate velocities. *Geochemistry, Geophysics, Geosystems*, *19*(3), 642–666. https://doi.org/10.1002/2017gc007112

Parang, S., Milne, G. A., Tarasov, L., Love, R., Yousefi, M., & Vacchi, M. (2024). Constraining models of glacial isostatic adjustment in eastern North America. *Quaternary Science Reviews*, *334*, 108708. https://doi.org/10.1016/j.quascirev.2024.108708

Paulson, A., Zhong, S., & Wahr, J. (2005). Modelling post-glacial rebound with lateral viscosity variations. *Geophysical Journal International*, *163*(1), 357–371. https://doi.org/10.1111/j.1365-246x.2005.02645.x

Peltier, W. R., & Andrews, J. T. (1976). Glacial-isostatic adjustment - I. The forward problem. *Geophysical Journal International*, *46*(3), 605–646. https://doi.org/10.1111/j.1365-246x.1976.tb01251.x

Peltier, W. R., Argus, D. F., & Drummond, R. (2015). Space geodesy constrains ice age terminal deglaciation: The global ICE-6G_C (VM5a) model [Dataset]. *Journal of Geophysical Research: Solid Earth*, *120*(1), 450–487. https://doi.org/10.1002/2014JB011176

Porritt, R. W., Becker, T. W., Boschi, L., & Auer, L. (2021). Multiscale, radially anisotropic shear wave imaging of the mantle underneath the contiguous United States through joint inversion of USArray and global data sets. *Geophysical Journal International*, *226*(3), 1730–1746. https://doi.org/10.1093/gji/ggab185

Reusen, J. M., Steffen, R., Steffen, H., Root, B. C., & van der Wal, W. (2023). Simulating horizontal crustal motions of glacial isostatic adjustment using compressible Cartesian models. *Geophysical Journal International*, *235*(1), 542–553. https://doi.org/10.1093/gji/ggad232

Ricard, Y., Doglioni, C., & Sabadini, R. (1991). Differential rotation between lithosphere and mantle: A consequence of lateral mantle viscosity variations. *Journal of Geophysical Research*, *96*(B5), 8407–8415. https://doi.org/10.1029/91jb00204

Sella, G. F., Stein, S., Dixon, T. H., Craymer, M., James, T. S., Mazzotti, S., & Dokka, R. K. (2007). Observation of glacial isostatic adjustment in "stable" North America with GPS. *Geophysical Research Letters*, *34*(2). https://doi.org/10.1029/2006gl027081
Snay, R. A., Freymueller, J. T., Craymer, M. R., Pearson, C. F., & Saleh, J. (2016). Modeling 3-D crustal velocities in the United States and Canada. *Journal of Geophysical Research: Solid Earth*, *121*(7), 5365–5388. https://doi.org/10.1002/2016jb012884
Steffen, H., Denker, H., & Müller, J. (2008). Glacial isostatic adjustment in Fennoscandia from GRACE data and comparison with geodynamical models. *Journal of Geodynamics*, *46*(3–5), 155–164. https://doi.org/10.1016/j.jog.2008.03.002
Steffen, H., Kaufmann, G., & Wu, P. (2006). Three-dimensional finite-element modeling of the glacial isostatic adjustment in Fennoscandia. *Earth and Planetary Science Letters*, *250*(1–2), 358–375. https://doi.org/10.1016/j.epsl.2006.08.003
Steffen, H., & Wu, P. (2014). The sensitivity of GNSS measurements in Fennoscandia to distinct three-dimensional upper-mantle structures. *Solid Earth*, *5*(1), 557–567. https://doi.org/10.5194/se-5-557-2014
Steffen, H., Wu, P., & Kaufmann, G. (2007). Sensitivity of crustal velocities in Fennoscandia to radial and lateral viscosity variations in the mantle. *Earth and Planetary Science Letters*, *257*(3–4), 474–485. https://doi.org/10.1016/j.epsl.2007.03.002
Steinberger, B., & Becker, T. W. (2018). A comparison of lithospheric thickness models. *Tectonophysics*, *746*, 325–338. https://doi.org/10.1016/j.tecto.2016.08.001
Tanaka, Y., Klemann, V., Martinec, Z., & Riva, R. (2011). Spectral-finite element approach to viscoelastic relaxation in a spherical compressible Earth: Application to GIA modelling. *Geophysical Journal International*, *184*(1), 220–234. https://doi.org/10.1111/j.1365-246x.2010.04854.x
Thrastarson, S., van Herwaarden, D. P., Noe, S., Josef Schiller, C., & Fichtner, A. (2024). REVEAL: A global full-waveform inversion model. *Bulletin of the Seismological Society of America*, *114*(3), 1392–1406. https://doi.org/10.1785/0120230273
Truesdell, C. (1953). Two measures of vorticity. *Journal of Rational Mechanics and Analysis*, *2*, 173–217. https://doi.org/10.1512/iumj.1953.2.52009
Turcotte, D. L., & Schubert, G. (2002). *Geodynamics* (2nd ed.). Cambridge Univ. Press.
van Summeren, J., Conrad, C. P., & Lithgow-Bertelloni, C. (2012). The importance of slab pull and a global asthenosphere to plate motions. *Geochemistry, Geophysics, Geosystems*, *13*(2). https://doi.org/10.1029/2011gc003873
van Calcar, C. J., Bernales, J., Berends, C. J., van der Wal, W., & van de Wal, R. S. W. (2025). Bedrock uplift reduces Antarctic sea-level contribution over next centuries. *Nature Communications*, *16*(1), 10512. https://doi.org/10.1038/s41467-025-66435-y
Van Calcar, C. J., Van De Wal, R. S., Blank, B., De Boer, B., & Van Der Wal, W. (2023). Simulation of a fully coupled 3D glacial isostatic adjustment–ice sheet model for the Antarctic ice sheet over a glacial cycle. *Geoscientific Model Development*, *16*(18), 5473–5492. https://doi.org/10.5194/gmd-16-5473-2023
van der Wal, W., Whitehouse, P. L., & Schrama, E. J. (2015). Effect of GIA models with 3D composite mantle viscosity on GRACE mass balance estimates for Antarctica. *Earth and Planetary Science Letters*, *414*, 134–143. https://doi.org/10.1016/j.epsl.2015.01.001
Vardić, K., Clarke, P. J., & Whitehouse, P. L. (2022). A GNSS velocity field for crustal deformation studies: The influence of glacial isostatic adjustment on plate motion models. *Geophysical Journal International*, *231*(1), 426–458. https://doi.org/10.1093/gji/ggac047
Wahr, J., & Zhong, S. (2013). Computations of the viscoelastic response of a 3D compressible Earth to surface loading: An application to Glacial Isostatic Adjustment in Antarctica and Canada. *Geophysical Journal International*, *192*(2), 557–572. https://doi.org/10.1093/gji/ggs030
Wang, H., & Wu, P. (2006). Effects of lateral variations in lithospheric thickness and mantle viscosity on glacially induced surface motion on a spherical, self-gravitating Maxwell Earth. *Earth and Planetary Science Letters*, *244*(3–4), 576–589. https://doi.org/10.1016/j.epsl.2006.02.026
Wang, H., Wu, P., & van der Wal, W. (2008). Using postglacial sea level, crustal velocities and gravity-rate-of-change to constrain the influence of thermal effects on mantle lateral heterogeneities. *Journal of Geodynamics*, *46*(3–5), 104–117. https://doi.org/10.1016/j.jog.2008.03.003
Watts, A. B. (2001). *Isostasy and flexure of the lithosphere*. Cambridge University Press.
Watts, A. B., Zhong, S. J., & Hunter, J. (2013). The behavior of the lithosphere on seismic to geologic timescales. *Annual Review of Earth and Planetary Sciences*, *41*(1), 443–468. https://doi.org/10.1146/annurev-earth-042711-105457
Wu, P. (2005). Effects of lateral variations in lithospheric thickness and mantle viscosity on glacially induced surface motion in Laurentia. *Earth and Planetary Science Letters*, *235*(3–4), 549–563. https://doi.org/10.1016/j.epsl.2005.04.038
Wu, P. (2006). Sensitivity of relative sea levels and crustal velocities in Laurentide to radial and lateral viscosity variations in the mantle. *Geophysical Journal International*, *165*(2), 401–413. https://doi.org/10.1111/j.1365-246x.2006.02960.x
Wu, P., & Peltier, W. R. (1982). Viscous gravitational relaxation. *Geophysical Journal International*, *70*(2), 435–485. https://doi.org/10.1111/j.1365-246x.1982.tb04976.x
Yousefi, M., Milne, G. A., & Latychev, K. (2021). Glacial isostatic adjustment of the Pacific Coast of North America: The influence of lateral Earth structure. *Geophysical Journal International*, *226*(1), 91–113. https://doi.org/10.1093/gji/ggab053
Yousefi, M., Milne, G. A., Love, R., & Tarasov, L. (2018). Glacial isostatic adjustment along the Pacific coast of central North America. *Quaternary Science Reviews*, *193*, 288–311. https://doi.org/10.1016/j.quascirev.2018.06.017
Yuan, T., & Zhong, S. (2025). Effects of glacial forcing on lithospheric motion and ridge spreading. *Nature*, *641*(8061), 1–7. https://doi.org/10.1038/s41586-025-08846-x
Yuan, T., Zhong, S., & A, G. (2025). CitcomSVE-3.0: A three-dimensional finite-element software package for modeling load-induced deformation and glacial isostatic adjustment for an Earth with a viscoelastic and compressible mantle [Software]. *Geoscientific Model Development*, *18*(5), 1445–1461. https://doi.org/10.5194/gmd-18-1445-2025
Zhong, S. (2001). Role of ocean-continent contrast and continental keels on plate motion, net rotation of lithosphere, and the geoid. *Journal of Geophysical Research*, *106*(B1), 703–712. https://doi.org/10.1029/2000jb900364
Zhong, S., Kang, K., A, G., & Qin, C. (2022). CitcomSVE: A three-dimensional finite element software package for modeling planetary mantle's viscoelastic deformation in response to surface and tidal loads [Software]. *Geochemistry, Geophysics, Geosystems*, *23*(10), .e2022GC010359. https://doi.org/10.1029/2022GC010359
Zhong, S., Paulson, A., & Wahr, J. (2003). Three-dimensional finite-element modelling of Earth's viscoelastic deformation: Effects of lateral variations in lithospheric thickness. *Geophysical Journal International*, *155*(2), 679–695. https://doi.org/10.1046/j.1365-246x.2003.02084.x